Open-Circuit Fault Diagnosis Method in NPC Rectifiers Using Fault-Assumed Strategy

Mingyun Chen and Yigang He, *Member, IEEE*

***Abstract*—This article proposes a new open-circuit (OC) fault diagnosis method for power switches in three-level neutral-point-clamped (NPC) rectifiers. This method is based on fault assumption by introducing a new voltage deviation for diagnosis, which is the difference between the switching-state-based voltage and the fault-assumed-based voltage, where the fault-assumed-based voltage is the estimated pole voltage when all inner switches are assumed to be in the OC state. After average and sum operations, diagnostic variables are developed from three-phase voltage deviations without extra hardware and precise modeling. Since the fault characteristics of each switch reflected by diagnostic variables are not changed by other concurrent OC faults, multiple-switch faults can be diagnosed in the same way as single-switch faults. As a result, the proposed method can detect both single-switch and multiple-switch faults without complex diagnostic rules and procedures. Besides, adaptive thresholds are designed by considering voltage imbalance, current amplitude, and power factor. Owing to the self-adjusting characteristics of thresholds, the proposed method provides reliable diagnostic results in various operating states of NPC rectifiers and has good robustness against transient changes. Experiments are performed to confirm its effectiveness and robustness.**

***Index Terms*—Fault assumption, fault diagnosis, fault identification, neutral-point-clamped rectifier, open-circuit fault.**

NOMENCLATURE

R_{xj}	Working range of switch S_{xj}.
I_{m}	Current amplitude.
M	Modulation index.
PF	Power factor.
δ	Phase difference between the rectifier current and voltage.
θ	Phase difference between the grid voltage and rectifier voltage.
φ	Phase difference between the rectifier current and grid voltage (power factor angle).
$v_{x\mathrm{o}}$	Switching-state-based pole voltage.
$v^*_{x\mathrm{o}}$	Fault-assumed-based pole voltage assuming S_{x2} and S_{x3} are in the OC state.
$\bar{v}_{x\mathrm{o}}$	Average $v_{x\mathrm{o}}$ in a switching period.
$\bar{v}^*_{x\mathrm{o}}$	Average $v^*_{x\mathrm{o}}$ in a switching period.
$\Delta\bar{v}_{x\mathrm{o}}$	Voltage deviation between $\bar{v}_{x\mathrm{o}}$ and $\bar{v}^*_{x\mathrm{o}}$.
$\Delta\bar{v}_{x\mathrm{o\_n}}$	Normalized $\Delta\bar{v}_{x\mathrm{o}}$ by dc bus voltages.
$\Delta\bar{v}_{x\mathrm{o\_sum}}$	Accumulation of $\Delta\bar{v}_{x\mathrm{o\_n}}$ in a half current cycle.
ε_{x1}	Small threshold for $\Delta\bar{v}_{x\mathrm{o\_sum}}$.
ε_{x2}	Large threshold for $\Delta\bar{v}_{x\mathrm{o\_sum}}$.
γ_x	Current angle of phase x.

Manuscript received 19 April 2022; accepted 7 June 2022. Date of publication 15 June 2022; date of current version 26 July 2022. This work was supported in part by the National Natural Science Foundation of China under Grants 51977153, 51977161, and 51577046, in part by the National Key Research and Development Plan under Grants 2020YFB0905905 and 2016YFF0102200, and in part by the State Key Program of National Natural Science Foundation of China under Grant 51637004. Recommended for publication by Associate Editor D. Zhang. (*Corresponding author: Yigang He.*)

The authors are with the School of Electrical Engineering and Automation, Wuhan University, Wuhan 430072, China (e-mail: mingyun.chen@whu.edu.cn; 18655136887@163.com).

Color versions of one or more figures in this article are available at https://doi.org/10.1109/TPEL.2022.3183075.

Digital Object Identifier 10.1109/TPEL.2022.3183075

I. INTRODUCTION

MULTILEVEL converters have significant advantages over two-level voltage source converters (VSCs), such as lower switching losses, better harmonic performance, and higher voltage capabilities [1]. They are primarily diffused in high-power medium-voltage industrial applications. One of the most used multilevel converters is the three-level neutral-point-clamped (3L-NPC) converter topology, which is a competitive topology in power supplies, renewable energy systems, and power utility interfacing applications [2]–[4].

A large number of power switches increases the probability that a switch fault occurs in an NPC converter but also enables an NPC converter to operate in a fault-tolerant mode [5]. In this respect, fault diagnosis, which is devoted to locating the faulty switch, is an indispensable step prior to fault-tolerant control. There are two cases of catastrophic faults involved in power switches: short-circuit (SC) faults and open-circuit (OC) faults [6]. SC faults are fatal to a converter system and are usually protected by hardware, such as circuit breakers and fuses. Conversely, OC faults, which are induced by bond wires lift-off/rupture or gate driver failure, usually do not lead to serious overcurrent. However, they deteriorate the power quality by bringing about ripples and distortion in currents and voltages. Subsequently, they may result in the secondary failure of other components. It is necessary to locate OC faults as quickly and accurately as possible to trigger the downtime for maintenance or the fault-tolerant mode in time.

A great deal of previous research into OC fault diagnosis focused on analyzing postfault currents in VSC-based drive systems [7]–[10]. These methods are simple in implementation but usually take a long execution time and have a limit in diagnosing OC faults of NPC converters. For NPC inverters, when OC faults occur in the upper (or lower) two switches of the same phase, the fault characteristics of currents are

similar. Traditional current-based methods cannot distinguish between these two faults [11]. This difficulty can be overcome by injecting underexcited reactive power or applying different modulation patterns, with the cost of increased diagnostic time and complexity [12], [13]. The current paths of NPC rectifiers are different from those of inverters. Outer switch faults hardly distort the current under unity power factor [14], [15]. It is not easy to detect these faults by currents.

Another type of fault diagnosis method is based on using extra measurable signals or adding measurement circuits [16]–[19]. These methods can be applied to both two- and three-level converters. In [19], three voltage sensors are added to an NPC inverter to monitor phase pole voltages. In this way, the changes in voltages caused by OC faults can be sensed more visually and immediately. This method is advantageous in diagnostic speed but not cost-effective. Besides, it is impractical to add sensors to high-power-density systems that require a low volume or a lightweight, and it is not simple and feasible to install extra sensors within an existent module-integrated converter.

The above methods can be classified as signal-based methods. Recently, model-based methods have received considerable scholarly attention. These methods construct the residual between the monitored signal and the estimated signal obtained from the mathematical model [20]–[23]. Several state-of-the-art model-based methods take advantage of phase-to-phase pole voltage deviations [24]–[26]. They are improved in detection speed compared with current-based methods and lower in cost compared with hardware-based methods. However, it is not easy to obtain voltage deviations accurately because the precise mathematical modeling of the converter is essentially required, and the current derivative operator, which is sensitive to noise, is involved.

The research on single-switch fault diagnosis has been thoroughly investigated. Since multiple-switch faults interact, it is not practical to directly apply these methods to diagnosing multiple-switch faults. The missed and false detection rate may increase if the single-switch fault diagnosis method is used when multiple-switch faults actually occur. For example, two switch faults may be misdiagnosed as another switch fault using the single-switch fault diagnosis method in [26], which is based on phase-to-phase voltage deviations. This is because one diagnostic variable may simultaneously show the opposite fault information of two switches, and the fault characteristics reflected by this diagnostic variable are offset.

Recently, more research has been interested in the multiple-switch fault diagnosis of VSCs. Some current-based and current-observer model-based methods can be improved to identify multiple-switch faults by adding new diagnostic variables and rules [27]–[29]. In [30], multiple-switch faults can be diagnosed in the same way as single-switch faults by using common-mode voltage residuals without adding diagnostic rules. However, this method does not consider the interaction of multiple-switch faults on residuals. Accordingly, misdiagnosis cannot be avoided when two faults have an effect simultaneously. In order to improve diagnostic accuracy, the polarity sequences of phase-to-phase pole voltage deviation are proposed in [25]. Since each fault combination has a unique sequence as the identifier, multiple-switch faults can be located by comparing the actual sequence with those identifiers. Hence, the location process is complex and takes a long time. In [31], a postfault current model is built to detect the second fault after the first fault has been identified. This method is useful for successive faults, but multiple postfault models are required for different fault conditions. Overall, these methods have a common problem in diagnosing multiple-switch faults. That is, the diagnostic complexity increases with the improvement of diagnostic capability.

Plenty of power switches make the multiple-switch fault diagnosis in NPC converters more challenging, but meanwhile provide more redundant states for fault-tolerant control of multiple-switch faults, especially in rectifiers where most currents flow through freewheeling diodes [14]. In [32], multiple-switch faults of two-level rectifiers can be fully or partly compensated by a modified space vector pulse width modulation (SVPWM), indicating a possibility of fault-tolerant control for multiple-switch faults of NPC rectifiers. In [33] and [34], research on fault-tolerant control for multiple-switch faults of NPC converters has been conducted. For these postfault operation strategies, the identification of multiple-switch faults is the basis. On the other hand, locating each faulty switch, regardless of postfault operation strategies, will be helpful to save the maintenance cost and shorten the downtime, especially in high-power applications where discrete power switching modules are used [19]. Therefore, further studies in diagnosing multiple-switch faults of NPC converters are necessary.

Moreover, distinguishing between inner switch faults and outer switch faults is another challenge for fault diagnosis in NPC rectifiers. First, the fault characteristics of outer switch faults are often imperceptible, especially under unity power factor. Second, outer switch faults present similar fault characteristics as inner switch faults if their effects expand. Some literature only considers inner switch faults under unity power factor because the rectifier can maintain stable operation with outer switch faults in this condition [34]–[36].

As discussed above, some problems remain to be solved for fault diagnosis in NPC rectifiers. In order to balance the diagnostic performance between short detection time, low hardware effort, and less dependence on precise modeling, a new diagnosis method is proposed in this article, with contributions listed as follows.

1) The fault-assumed-based voltage deviations are proposed as the diagnostic variables, providing new thinking for fault diagnosis. They can be obtained without precise modeling and additional measurement circuits, making the diagnosis more reliable and cost-effective.
2) By designing adaptive thresholds, the diagnosis method is more robust against voltage imbalance and load variation, and can be applied to various operating states of NPC rectifiers covering different current amplitudes (modulation indexes) and power factors.
3) The proposed diagnostic procedure is simple and applicable to both single-switch and multiple-switch faults in NPC rectifiers. Specifically, owing to the proposed diagnostic variables that minimize the interaction of multiple fault characteristics, the identification method of

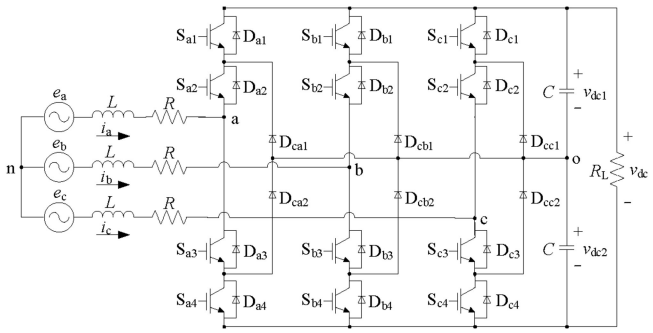

Fig. 1. Schematic of three-phase 3L-NPC rectifier topology.

multiple-switch faults is the same as that of single-switch faults, reducing the diagnostic complexity and improving the diagnostic accuracy.

In this article, the diagnostic performance of inner switch faults is the primary concern, and distinguishing between inner switch faults and outer switch faults is also one of the concerns when outer switch faults are accessible.

The rest of this article is organized as follows. In Section II, the average voltage deviation based on fault assumption is proposed. In Section III, the characteristics of voltage deviations in different fault conditions are analyzed. In Section IV, the proposed fault diagnosis method is elaborated, including the diagnostic variables and the threshold setting. In Section V, the experimental validation is carried out. Finally, Section VI concludes this article.

II. Voltage Deviation Based on Fault Assumption

A. Proposed Fault-Assumed-Based Voltage

A typical three-phase 3L-NPC rectifier system is described in Fig. 1. Power semiconductors in NPC rectifiers are divided into outer switches (S_{x1} and S_{x4}) and inner switches (S_{x2} and S_{x3}) in this article ($x \in \{a, b, c\}$). As illustrated in Fig. 2, there are six current paths according to current directions and switching states ([P], [O], [N]) in the normal condition.

For simplicity, the analysis is carried out by assuming that $v_{dc1} = v_{dc2} = v_{dc}/2$. It can be deduced from Fig. 2 that the pole voltage of phase a in the normal condition (called switching-state-based voltage) can be calculated as follows:

$$v_{ao} = s_a \cdot v_{dc}/2 \tag{1}$$

where s_a is the switching signal of phase a. $s_a = 1$, $s_a = 0$, and $s_a = -1$ represent the switching state [P], [O], and [N] in Fig. 2, respectively.

OC faults in phase a are chosen as examples. OC faults in the upper two switches (S_{a1} and S_{a2}) only affect the system when $i_a < 0$. If an OC fault occurs in S_{a1}, the negative current path of phase a with the switching state [P] changes from Fig. 2(a) to (b). Meanwhile, the pole voltage of phase a changes from $v_{dc}/2$ to 0. If an OC fault occurs in S_{a2}, the negative current path of phase a with the switching state [P] changes from Fig. 2(a) to (c), and the negative current path of phase a with the switching

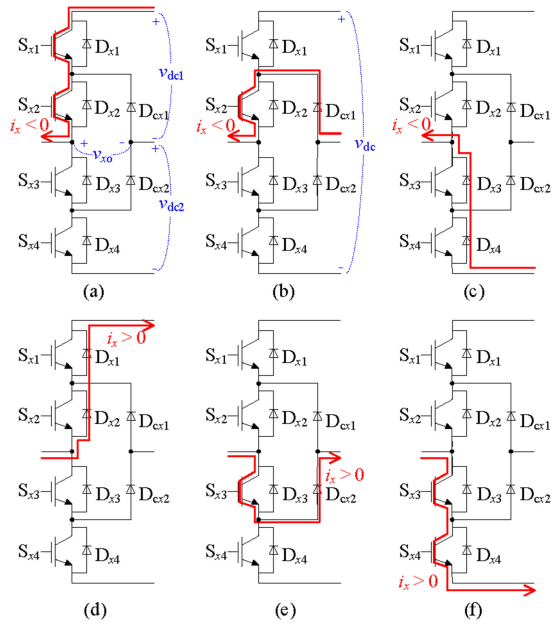

Fig. 2. Current paths in the normal operation of NPC rectifiers. (a) $i_x < 0$ with switching state [P]. (b) $i_x < 0$ with switching state [O]. (c) $i_x < 0$ with switching state [N]. (d) $i_x > 0$ with switching state [P]. (e) $i_x > 0$ with switching state [O]. (f) $i_x > 0$ with switching state [N].

state [O] changes from Fig. 2(b) to (c). Meanwhile, the pole voltage of phase a changes from $v_{dc}/2$ or 0 to $-v_{dc}/2$. Besides, OC faults may result in serious current distortion. For OC faults in S_{a1} and S_{a2}, the negative half-cycle of i_a is distorted with the zero-current condition possibly appearing for a long time. In the zero-current condition, phase a can be regarded as disconnected from the bridge arm. According to [21], the pole voltage of phase a can be derived as follows:

$$v_{ao} = (3e_a + V_{bo} + V_{co})/2, \quad i_a = 0 \tag{2}$$

where V_{bo} and V_{co} are the reference voltages given by the control loop.

OC faults in the lower two switches (S_{a3} and S_{a4}) can be analyzed in the same way. The difference is that S_{a3} and S_{a4} faults only affect the system when $i_a > 0$. S_{a3} fault changes the pole voltage to $v_{dc}/2$ with the switching state [N] or [O], and S_{a4} fault change the pole voltage to 0 with the switching state [N]. Besides, the positive half-cycle of i_a is distorted with the zero-current condition.

As a result, the postfault current can be divided into three parts: 1) $i_a > 0$; 2) $i_a = 0$; and 3) $i_a < 0$. By considering inner switch faults (assuming that both S_{a2} and S_{a3} are in the OC state), the pole voltage of phase a (called fault-assumed-based voltage) can be expressed as follows:

$$v_{ao}^* = \begin{cases} v_{dc}/2, & i_a > 0 \\ (3e_a + V_{bo} + V_{co})/2, & i_a = 0 \\ -v_{dc}/2, & i_a < 0. \end{cases} \tag{3}$$

In conclusion, the switching-state-based voltage defined by (1) is the expected pole voltage in the normal condition, and the proposed fault-assumed-based voltage defined by (3) is the

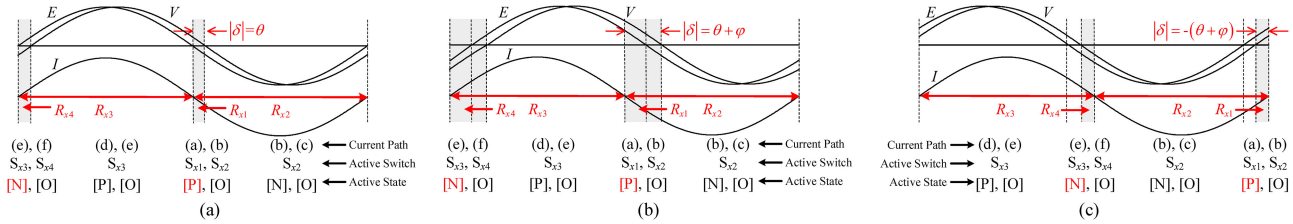

Fig. 3. Current paths of Fig. 2, active switches, and active switching states in different ranges of a current cycle. (a) When PF $= 1$ ($\varphi = 0$). (b) When PF < 1 ($\varphi > 0$). (c) When PF < 1 ($\varphi < 0$).

estimated pole voltage when inner switches are supposed to be in the OC state. The voltage deviation between them provides new thinking for fault diagnosis.

B. Average Voltage Deviation

Since the sampling and calculation are discretized, the average value of variable y in a switching/sampling period (T_s) is defined as follows:

$$Y[n] = (y[n-1] + y[n])/2 \tag{4}$$

where $y[n]$ represents the value of variable y in the nth switching/sampling point.

According to (1), the average value of the switching-state-based voltage can be written as follows:

$$\begin{aligned}\bar{v}_{\mathrm{ao}}[n] &= \bar{s}_{\mathrm{a}}[n-1] \cdot V_{\mathrm{dc}}[n]/2 \\ &= (D_{\mathrm{Pa}}[n-1] - D_{\mathrm{Na}}[n-1]) \cdot V_{\mathrm{dc}}[n]/2\end{aligned} \tag{5}$$

where V_{dc} is the average value of v_{dc} in T_s, $\bar{s}_\mathrm{a}$ represents the average switching signal in T_s , and D_{Pa}, D_{Oa}, and D_{Na} are the duty cycles of [P], [O], and [N].

Since $V_{\mathrm{ao}} + V_{\mathrm{bo}} + V_{\mathrm{co}} = 0$ in three-phase symmetrical systems, the average value of the fault-assumed-based voltage can be derived from (3) as follows:

$$\bar{v}^*_{\mathrm{ao}}[n] = \begin{cases} V_{\mathrm{dc}}[n]/2, & I_{\mathrm{a}}[n] > 0 \\ (3E_{\mathrm{a}}[n] - V_{\mathrm{ao}}[n-1])/2, & I_{\mathrm{a}}[n] = 0 \\ -V_{\mathrm{dc}}[n]/2, & I_{\mathrm{a}}[n] < 0 \end{cases} \tag{6}$$

where E_a and I_a are the average values of e_a and i_a in T_s.

According to (5) and (6), the average voltage deviation is obtained by the following:

$$\Delta\bar{v}_{\mathrm{ao}}[n] = \bar{v}_{\mathrm{ao}}[n] - \bar{v}^*_{\mathrm{ao}}[n]. \tag{7}$$

III. Voltage Deviation Characteristics in Various Fault Conditions

This section analyzes the severity of inner switch faults and outer switch faults affected by current amplitude (I_m), modulation index (M), and power factor (PF), as well as the characteristics of voltage deviation in such fault conditions.

A. Working Ranges of Switches in Normal Condition

As shown in Fig. 3, each switch has a working range where it can form the current path. The length of working ranges for inner switches (R_{x2} and R_{x3}) is as long as a half current cycle with zero crossing as the limit, whereas the length and location of working ranges for outer switches (R_{x1} and R_{x4}) depend on the phase difference (δ) between the rectifier current (I) and the rectifier voltage (V). Given that the rectifier may operate under nonunity power factor, δ consists of the phase differences: θ and φ [15]. θ is the phase difference between the grid voltage (E) and the rectifier voltage (V). φ is the power factor angle (PF $= \cos\varphi$), which is the phase difference between the rectifier current (I) and the grid voltage (E).

When PF $= 1$, δ equals θ ($\theta > 0$) and varies with I_m and M as follows [15]:

$$\theta = \tan^{-1}\left(\frac{\omega L I_{\mathrm{m}}}{E_{\mathrm{m}}}\right) = \sin^{-1}\left(\frac{\sqrt{3}\omega L I_{\mathrm{m}}}{M v_{\mathrm{dc}}}\right) \tag{8}$$

where $\omega = 2\pi/T$, and T is the fundamental period. In (8), the ac side resistance is neglected. It can be inferred that θ increases with a rise in I_m and a drop in M. However, θ is usually negligible when PF $= 1$. That is, the length of R_{x1} (or R_{x4}) is short. Fig. 3(a) reveals that the location of R_{x1} (or R_{x4}) is at the beginning of the negative (or positive) half-cycle current.

When PF < 1, δ is equal to $\theta + \varphi$ and significantly affected by PF. If $\varphi > 0$ (the current phase precedes the grid voltage phase), the length of R_{x1} (or R_{x4}) is longer, and its location is at the beginning of the negative (or positive) half-cycle current, as shown in Fig. 3(b). If $\varphi < 0$ (the current phase lags behind the grid voltage phase), the length of R_{x1} (or R_{x4}) can be shorter or longer, depending on the absolute value of $\theta + \varphi$. If $\theta + \varphi > 0$, the location of R_{x1} (or R_{x4}) is at the beginning of the negative (or positive) half-cycle current. If $\theta + \varphi < 0$, the location of R_{x1} (or R_{x4}) is at the end of the negative (or positive) half-cycle current, as shown in Fig. 3(c).

If an OC fault occurs in a switch within its working range, the current cannot flow through the faulty switch, inducing the distortion in the current and the variation in the voltage deviation. The more extended working range of a switch indicates a more significant impact of its OC fault on the system. For this reason, improving the diagnostic accuracy and speed of inner switch faults is the main objective of the proposed diagnosis method. Compared with inner switch faults, outer switch faults are not fatal and often unobservable under unity power factor due to their short working ranges. In fact, NPC rectifiers can maintain stable dc bus voltages with only six inner switches under unity power factor, which is known as the reduced-parts-count structure [36]. However, outer switch faults have to be considered when the working ranges of outer switches extend depending on the

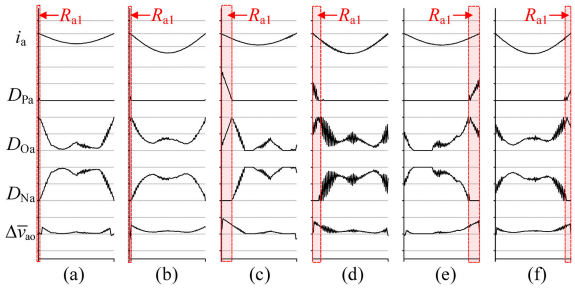

Fig. 4. Normal condition when $i_a \leq 0$. (a) $\varphi = 0$ with small I_m. (b) $\varphi = 0$ with large I_m. (c) $\varphi > 0$ with small I_m. (d) $\varphi > 0$ with large I_m. (e) $\varphi < 0$ with small I_m. (f) $\varphi < 0$ with large I_m.

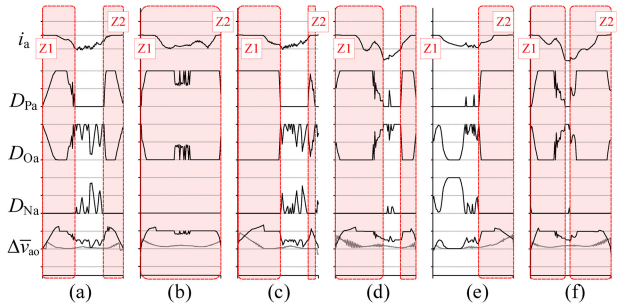

Fig. 5. S_{a2} fault condition when $i_a \leq 0$ (grey lines refers to normal conditions in Fig. 4). (a) $\varphi = 0$ with small I_m. (b) $\varphi = 0$ with large I_m. (c) $\varphi > 0$ with small I_m. (d) $\varphi > 0$ with large I_m. (e) $\varphi < 0$ with small I_m. (f) $\varphi < 0$ with large I_m.

operating states of the system. Therefore, if outer switch faults are observable, distinguishing between inner switch faults and outer switch faults is also one of the concerns of this article.

To achieve the two goals, analyzing the characteristics of voltage deviations is essential in terms of various operating states and different fault conditions.

B. Voltage Deviation in Normal Condition

The characteristics of voltage deviations are different within and out of the working ranges of outer switches. According to (5)–(7), $\Delta\bar{v}_{ao}$ can be expressed as follows:

$$\Delta\bar{v}_{ao} = \begin{cases} -(2D_{Na} + D_{Oa}) \cdot \frac{V_{dc}}{2}, & I_a > 0 \\ (2D_{Pa} + D_{Oa}) \cdot \frac{V_{dc}}{2}, & I_a < 0. \end{cases} \tag{9}$$

It can be inferred that $\Delta\bar{v}_{ao} \neq 0$ in the normal condition. When $I_a > 0$, $\Delta\bar{v}_{ao} < 0$. When $I_a < 0$, $\Delta\bar{v}_{ao} > 0$. It should be mentioned that normal currents do not remain zero for a long time, so the situation that $I_a = 0$ is not considered in (9).

When I_a<0, $\Delta\bar{v}_{ao}$ depends on D_{Pa} and D_{Oa}. Within R_{a1}, $D_{Pa} + D_{Oa} = 1$, and accordingly, $\Delta\bar{v}_{ao} = (1 + D_{Pa}) \cdot V_{dc}/2$, which is larger than $V_{dc}/2$. Out of R_{a1}, $D_{Pa} = 0$, and accordingly, $\Delta\bar{v}_{ao} = D_{Oa} \cdot V_{dc}/2$ which is smaller than $V_{dc}/2$. On this basis, $\Delta\bar{v}_{ao}$ is large within R_{a1} and small out of R_{a1}. As mentioned before, the length of R_{a1} is equal to $|\theta + \varphi|$ and affected by I_m, M, and PF. If NPC rectifiers generate large I_m with small M, θ increases and the length of R_{a1} changes, as shown in Fig. 4. However, these variations are usually slight. Large I_m mainly manifests as higher D_{Oa} and lower D_{Na} rather than a marked extension of R_{a1}. According to (9), $\Delta\bar{v}_{ao}$ slightly increases in the negative half-cycle of i_a, as illustrated in Fig. 4(b), (d), and (f) [compared with Fig. 4(a), (c), and (e), respectively]. The decline in *PF* has a significant effect on R_{a1}. If $\varphi > 0$, R_{a1} clearly extends as analyzed before. Compared with Fig. 4(a), D_{Pa} and $\Delta\bar{v}_{ao}$ increase within the longer R_{a1} in Fig. 4(c). If $\varphi < 0$, R_{a1} can be shorter or longer, as analyzed before. Compared with Fig. 4(a), D_{Pa} and $\Delta\bar{v}_{ao}$ increase within the longer R_{a1} in Fig. 4(e). Unlike Fig. 4(a) and (c), the location of R_{a1} is at the end in Fig. 4(e).

When $I_a > 0$, $\Delta\bar{v}_{ao}$ has similar characteristics. $|\Delta\bar{v}_{ao}|$ ($\Delta\bar{v}_{ao} < 0$) is large within R_{a4} depending on D_{Na} and small out of R_{a4} depending on D_{Oa}, and meanwhile, affected by I_m, M, and PF.

C. Voltage Deviation in Inner Switch Fault Condition

S_{a2} fault leads to severe current distortion with two zero sections at the beginning and the end of R_{a2} (labeled as Z1 and Z2, respectively). Given Z1 and Z2, $\Delta\bar{v}_{ao}$ can be derived as follows (see the Appendix):

$$\Delta\bar{v}_{ao} = \begin{cases} -(2D_{Na} + D_{Oa}) \cdot \frac{V_{dc}}{2}, & I_a > 0 \\ -\frac{3}{2}\left(E_a - \frac{V_{dc}}{T_s}\sum k_{V_i} t_{V_i}\right), & I_a = 0 \\ (2D_{Pa} + D_{Oa}) \cdot \frac{V_{dc}}{2}, & I_a < 0. \end{cases} \tag{10}$$

When $I_a > 0$ (out of R_{a2}), S_{a2} fault does not affect the system, and $\Delta\bar{v}_{ao}$ is the same as its normal value.

When $I_a < 0$, $\Delta\bar{v}_{ao}$ is large within R_{a1} depending on D_{Pa} and small out of R_{a1} depending on D_{Oa}, as analyzed before. The most striking differences between the inner switch fault condition and the normal condition are the extension of R_{a1} and the increase in D_{Pa}, as shown in Fig. 5. Thus, $\Delta\bar{v}_{ao}$ remarkably increases within the longer R_{a1} in case of S_{a2} fault, which can be confirmed by comparing black lines (S_{a2} fault) with grey lines (normal condition) in Fig. 5.

When $I_a = 0$, $\Delta\bar{v}_{ao}$ is in a steady upward or downward trend with the current angle. According to (10), $\Delta\bar{v}_{ao}$ depends on the grid voltage and the average voltage vector applied in a switching period. Eighteen nonzero voltage vectors $\boldsymbol{V}_i$ ($i = 1, 2, \ldots, 18$) with diverse magnitudes and angles constitute a voltage vector diagram, as depicted in Fig. 6. In Z1, the voltage vectors that play the main role are $\boldsymbol{V}_2$, $\boldsymbol{V}_7$, and $\boldsymbol{V}_{14}$. These vectors contain the switching state [P] in phase a. Supposing that a switching period consists of only one of these voltage vectors, $\Delta\bar{v}_{ao}$ takes the values of $3|E_a|/2 + V_{dc}/4$, $3|E_a|/2 + 3V_{dc}/4$, and $3|E_a|/2 + V_{dc}/2$, respectively, for $\boldsymbol{V}_2$, $\boldsymbol{V}_7$, and $\boldsymbol{V}_{14}$ (see the Appendix). Consequently, $\Delta\bar{v}_{ao}$ gradually increases with the decrease in E_a ($E_a < 0$), as demonstrated in Fig. 5. Furthermore, a large amplitude of e_a makes $\Delta\bar{v}_{ao}$ increase faster in a shorter Z1. If grid voltages are unbalanced, the fault characteristics of currents and voltage deviations in different phases might differ slightly. A similar analysis can be applied to Z2 in which $\Delta\bar{v}_{ao}$ gradually decreases with the increase in E_a.

Besides, I_m, M, and PF affect the severity of inner switch faults. Large I_m with small M makes R_{a1} extend heavily, and $\Delta\bar{v}_{ao}$ remains at its maximum for almost the entire half-cycle,

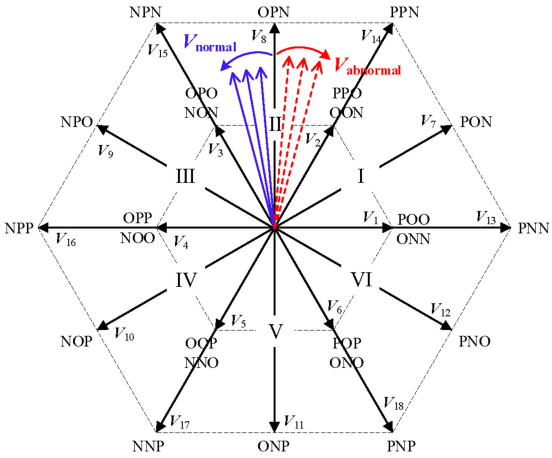

Fig. 6. Voltage vector diagram of three-level SVPWM.

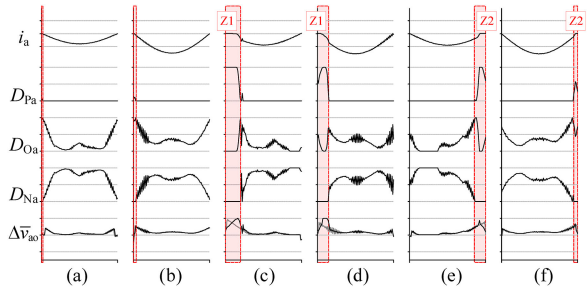

Fig. 7. S_{a1} fault condition when $i_a \leq 0$ (grey lines refers to normal conditions in Fig. 4). (a) $\varphi = 0$ with small I_m. (b) $\varphi = 0$ with large I_m. (c) $\varphi > 0$ with small I_m. (d) $\varphi > 0$ with large I_m. (e) $\varphi < 0$ with small I_m. (f) $\varphi < 0$ with large I_m.

as illustrated in Fig. 5(b), (d), and (f) [compared with Fig. 5(a), (c), and (e), respectively]. When PF declines, R_{a1} extends in different locations depending on the polarity of φ. If $\varphi > 0$, Z1 is longer than Z2. Compared with Fig. 5(a), R_{a1} mainly extends in Z1 in Fig. 5(c). If $\varphi < 0$ with small PF, Z2 is longer than Z1. Compared with Fig. 5(a), R_{a1} mainly extends in Z2 in Fig. 5(e). Thereby, the maximum value of $\Delta\bar{v}_{ao}$ is concentrated in different locations.

Likewise, a conclusion can be drawn that if an OC fault occurs in S_{a3}, $\Delta\bar{v}_{ao}$ ($\Delta\bar{v}_{ao} < 0$) dramatically decreases when $I_a \geq 0$ (within R_{a3}) compared with its normal value. The extension of R_{a4} and the increase in D_{Na} are the main reasons.

D. Voltage Deviation in Outer Switch Fault Condition

The expression for $\Delta\bar{v}_{ao}$ in case of outer switch faults is the same as (10). S_{a1} fault only deteriorates the system performance within R_{a1}. Hence, when $I_a > 0$, $\Delta\bar{v}_{ao}$ is the same as its normal value.

When $I_a \leq 0$, the difference in $\Delta\bar{v}_{ao}$ between the S_{a1} fault condition and the normal condition is mainly caused by the increase in D_{Pa}. As shown in Fig. 7, R_{a1} does not extend obviously compared with the normal condition in Fig. 4. Therefore, $\Delta\bar{v}_{ao}$ is the same as its normal value most of the time, which can be confirmed by comparing black lines (S_{a1} fault) with grey lines (normal condition) in Fig. 7. When PF $= 1$, D_{Pa} slightly increases within R_{a1}. Accordingly, the difference in $\Delta\bar{v}_{ao}$ between the S_{a1} fault condition and the normal condition is imperceptible even if I_m increases, as displayed in Fig. 7(b). When PF < 1, S_{a1} fault exhibits similar postfault characteristics as S_{a2} fault. For example, there is a long duration of zero currents and a noticeable increase in D_{Pa}. By comparing black lines (S_{a1} fault) with grey lines (normal condition) in Fig. 7(c) and (e), it can be seen that $\Delta\bar{v}_{ao}$ is larger than its normal value within R_{a1}, which makes it difficult to distinguish between S_{a1} fault and S_{a2} fault. However, as mentioned before, S_{a1} fault does not appreciably make R_{a1} extend as S_{a2} fault does, which is the main difference between S_{a1} fault and S_{a2} fault. In addition, it can be inferred by comparing Fig. 7(d) with (c) that increasing I_m does not further deteriorate the postfault performance and does not make the postfault characteristics more pronounced when PF < 1. The difference in $\Delta\bar{v}_{ao}$ between the S_{a1} fault condition (black line) and the normal condition (grey line) in Fig. 7(d) is similar to that in Fig. 7(c).

Likewise, a conclusion can be drawn that if an OC fault occurs in S_{a4}, $\Delta\bar{v}_{ao}$ ($\Delta\bar{v}_{ao} < 0$) slightly decreases within R_{a4} compared with its normal value. The increase in D_{Na} within R_{a4} is the main reason.

The reason why R_{a1} extends and D_{Pa} increases in case of S_{a1} fault or S_{a2} fault can be analyzed from the perspective of voltage vectors. As depicted in Fig. 6, when i_a leaves the positive half-cycle, the reference voltage vector $\boldsymbol{V}$ (solid line) rotates forward from Sector II to Sector III in the normal condition. Whereas in case of S_{a1} fault or S_{a2} fault, $\boldsymbol{V}$ (dash line) rotates inversely from Sector II to Sector I with the increase in its amplitude by the control loop regulation [37]. Due to the inverse rotation of $\boldsymbol{V}$, θ increases, resulting in the extension of R_{a1}. Affected by the counterrotating $\boldsymbol{V}$ and its rising amplitude, the dwell time for voltage vectors [PPN], [PON], and [PNN] is longer, inducing the increase in D_{Pa}. Meanwhile, redundant small voltage vectors contribute to the increase in D_{Pa}. The P-type voltage vector [POO] and the N-type voltage vector [ONN] are a pair of the redundant small voltage vector $\boldsymbol{V}_1$. If the neutral-point voltage is balanced, the dwell time for a pair of the redundant small vector can be equally distributed between its P- and N-type voltage vectors in a switching period to minimize the neutral-point voltage. However, S_{a1} fault or S_{a2} fault will force the input terminal of phase a to connect to the negative dc bus for a long time. The lower capacitor is more charged than the upper capacitor, resulting in the unbalanced neutral-point voltage. If a neutral-point voltage balancing control is adopted based on redistributing the dwell time for P- and N-type voltage vectors, the dwell time for P-type voltage vectors increases. As a result, P-type voltage vectors [PPO] and [POO] make D_{Pa} increase under the effect of the counterrotating $\boldsymbol{V}$. A similar analysis is valid for the situation that i_a leaves the negative half-cycle.

IV. Proposed Fault Diagnosis Method

A. Diagnostic Variables

In previous sections, $\Delta\bar{v}_{ao}$ is discussed as an example. Since $\Delta\bar{v}_{ao}$ is obtained by signals from phase a and dc side. $\Delta\bar{v}_{bo}$ and $\Delta\bar{v}_{co}$ can be derived in the same way. Therefore, three-phase

voltage deviations are independent of each other. $\Delta\bar{v}_{\mathrm{ao}}$ only presents the fault characteristics of switches from phase a. Similarly, $\Delta\bar{v}_{\mathrm{bo}}$ and $\Delta\bar{v}_{\mathrm{co}}$ only present the fault characteristics of switches from phase b and phase c, respectively. Each faulty switch can be identified by one voltage deviation of the corresponding phase, regardless of other deviations. Therefore, taking three-phase voltage deviations as diagnostic variables can minimize the interaction of multiple fault characteristics and avoid misdiagnosis. However, some improvements should be made on voltage deviations as follows to reduce the effect of a single sampling error on calculation and make the postfault characteristics easier to be distinguished.

After OC faults occur, upper and lower capacitor voltages are greatly unbalanced. Given such concerns, the expression for the average switching-state-based voltage is improved by the following:

$$\bar{v}_{\mathrm{ao}}[n] = D_{\mathrm{Pa}}[n-1]\cdot V_{\mathrm{dc1}}[n] - D_{\mathrm{Na}}[n-1]\cdot V_{\mathrm{dc2}}[n] \quad (11)$$

where $D_{\mathrm{Pa}} = D_{\mathrm{a1}}$ and $D_{\mathrm{Na}} = D_{\mathrm{a4}}$. D_{a1} and D_{a4} are the duty cycles of $\mathrm{S_{a1}}$ switching signal and $\mathrm{S_{a4}}$ switching signal, which can be obtained from the SVPWM module, and V_{dc1} and V_{dc2} are the average values of v_{dc1} and v_{dc2} in T_{s}.

Given measurement errors and noise disturbances, the current is not precisely zero in Z1 and Z2. A small threshold (h) is devised to determine the expression for the average fault-assumed-based voltage, which is modified as follows:

$$\bar{v}^{*}_{\mathrm{ao}}[n] = \begin{cases} V_{\mathrm{dc1}}[n], & I_{\mathrm{a}}[n] > h \\ \left(3E_{\mathrm{a}}[n] - V_{\mathrm{ao}}[n-1]\right)/2, & |I_{\mathrm{a}}[n]| \le h \\ -V_{\mathrm{dc2}}[n], & I_{\mathrm{a}}[n] < -h \end{cases} \quad (12)$$

where h can be defined as a low percentage of I_{m}. It is governed by several factors, such as switching frequency, current sensor offset, and current signal-to-noise ratio [38].

Besides, to make the diagnostic variable independent of the load, the average voltage deviation is normalized by dc bus voltages as follows:

$$\Delta\bar{v}_{\mathrm{ao\_n}}[n] = \frac{\bar{v}_{\mathrm{ao}}[n] - \bar{v}^{*}_{\mathrm{ao}}[n]}{V_{\mathrm{dc1}}[n] + V_{\mathrm{dc2}}[n]}. \quad (13)$$

The analysis in Section III indicates that the polarity of $\Delta\bar{v}_{\mathrm{ao\_n}}$ in a half current cycle is the same. In order to present the variation in $\Delta\bar{v}_{\mathrm{ao\_n}}$ caused by OC faults more directly, the diagnostic variable can be devised by adding up $\Delta\bar{v}_{\mathrm{ao\_n}}$ in every half current cycle as follows:

$$\Delta\bar{v}_{\mathrm{ao\_sum}}[n] = \begin{cases} \Delta\bar{v}_{\mathrm{ao\_sum}}[n-1] + \Delta\bar{v}_{\mathrm{ao\_n}}[n], & \gamma_{\mathrm{a}}[n] \neq i\cdot\pi \\ 0, & \gamma_{\mathrm{a}}[n] = i\cdot\pi \end{cases}, \quad i \in \{0,\ 1\} \quad (14)$$

where γ_{a} ($\gamma_{\mathrm{a}} \in [0, 2\pi]$) is the current angle of phase a, which can be deduced from the grid voltage angle and the power factor angle. Similarly, diagnostic variables of phase b ($\Delta\bar{v}_{\mathrm{bo\_sum}}$) and phase c ($\Delta\bar{v}_{\mathrm{co\_sum}}$) can be obtained.

B. Threshold Setting

The threshold setting is a contributing component of the diagnosis method. Unlike model-based methods, the proposed diagnostic variables are theoretically nonzero in the normal condition. It can be deduced from Section III that $\Delta\bar{v}_{\mathrm{ao\_sum}}$ is smaller than zero and in the downward trend with the current angle when $\gamma_{\mathrm{a}} \in [0,\ \pi)$, and $\Delta\bar{v}_{\mathrm{ao\_sum}}$ is larger than zero and in the upward trend with the current angle when $\gamma_{\mathrm{a}} \in [\pi,\ 2\pi)$. The values of diagnostic variables must be estimated in the normal condition for setting thresholds.

According to (9), $\Delta\bar{v}_{\mathrm{ao\_sum}}$ is the accumulation of D_{Pa} (or D_{Na}) and $D_{\mathrm{Oa}}/2$ in a half current cycle. As analyzed before, the extension of R_{a1} (or R_{a4}) and the increase in D_{Pa} (or D_{Na}) are the main reasons for the difference in diagnostic variables between normal and fault conditions. Therefore, $D_{\mathrm{Oa}}/2$ is set as the basis for thresholds as follows:

$$D_{\mathrm{a}}[n-1] = D_{\mathrm{Oa}}[n-1]/2 \quad (15)$$

where $D_{\mathrm{Oa}} = 1 - D_{\mathrm{a1}} - D_{\mathrm{a4}}$.

In (15), the upper and lower capacitor voltages are assumed to be equal. In fact, they are not the same value and usually fluctuate even in the normal condition. This factor should be considered in the threshold setting. Given the switching loss, there is no transition between [P] and [N] in a switching period, which means at least one of D_{Pa} and D_{Na} is zero in a switching period. Specifically, $D_{\mathrm{Pa}} + D_{\mathrm{Oa}} = 1$ or $D_{\mathrm{Na}} + D_{\mathrm{Oa}} = 1$ in a switching period. According to (11)–(13), $\Delta\bar{v}_{\mathrm{ao\_n}}$ has two expressions when $\gamma_{\mathrm{a}} \in [\pi,\ 2\pi)$ (i.e., $I_{\mathrm{a}} < -h$ in the normal condition)

If $D_{\mathrm{Pa}}[n-1] = 0$,

$$\Delta\bar{v}_{\mathrm{ao\_n}}[n] = \frac{-D_{\mathrm{Na}}[n-1]\cdot V_{\mathrm{dc2}}[n] + V_{\mathrm{dc2}}[n]}{V_{\mathrm{dc1}}[n] + V_{\mathrm{dc2}}[n]} = \frac{D_{\mathrm{Oa}}[n-1]\cdot V_{\mathrm{dc2}}[n]}{V_{\mathrm{dc1}}[n] + V_{\mathrm{dc2}}[n]}. \quad (16)$$

If $D_{\mathrm{Na}}[n-1] = 0$,

$$\Delta\bar{v}_{\mathrm{ao\_n}}[n] = \frac{D_{\mathrm{Pa}}[n-1]\cdot V_{\mathrm{dc1}}[n] + V_{\mathrm{dc2}}[n]}{V_{\mathrm{dc1}}[n] + V_{\mathrm{dc2}}[n]} = D_{\mathrm{Pa}}[n-1] + \frac{D_{\mathrm{Oa}}[n-1]\cdot V_{\mathrm{dc2}}[n]}{V_{\mathrm{dc1}}[n] + V_{\mathrm{dc2}}[n]}. \quad (17)$$

For (16) and the latter term of (17), if $V_{\mathrm{dc1}}[n] = V_{\mathrm{dc2}}[n]$, the equation is equal to $D_{\mathrm{Oa}}[n-1]/2$; if $V_{\mathrm{dc1}}[n] > V_{\mathrm{dc2}}[n]$, the equation is smaller than $D_{\mathrm{Oa}}[n-1]/2$; if $V_{\mathrm{dc1}}[n] < V_{\mathrm{dc2}}[n]$, the equation is larger than $D_{\mathrm{Oa}}[n-1]/2$. A similar analysis is valid when $\gamma_{\mathrm{a}} \in [0,\ \pi)$(i.e., $I_{\mathrm{a}} > h$ in the normal condition). Therefore, $\Delta\bar{v}_{\mathrm{ao\_n}}$ is affected by the voltage imbalance. Define the voltage imbalance factor as follows:

$$\lambda[n] = \frac{V_{\mathrm{dc2}}[n] - V_{\mathrm{dc1}}[n]}{V_{\mathrm{dc1}}[n] + V_{\mathrm{dc2}}[n]}. \quad (18)$$

Accordingly, the basis for thresholds in (15) is modified as follows:

$$D_{\mathrm{a}}[n-1] = \begin{cases} (1-\lambda[n])\cdot D_{\mathrm{Oa}}[n-1]/2, & \gamma_{\mathrm{a}}[n] \in [0,\ \pi) \\ (1+\lambda[n])\cdot D_{\mathrm{Oa}}[n-1]/2, & \gamma_{\mathrm{a}}[n] \in [\pi,\ 2\pi) \end{cases}. \quad (19)$$

When $\gamma_{\rm a} \in [\pi,\ 2\pi)$, the estimated accumulation of $D_{\rm Pa}$ is a decisive factor for detecting OC faults, which relies on the range ,where $D_{\rm Pa} \neq 0$ (i.e., $R_{\rm a1}$). The duration of $R_{\rm a1}$ decided by δ is calculated as follows:

$$T_\delta[n] = |\delta[n]| \cdot \frac{T}{2\pi} = |\theta[n] + \varphi[n]| \cdot \frac{T}{2\pi}. \tag{20}$$

One of the simple ways to obtain T_δ can be expressed as follows:

$$\theta[n] = \tan^{-1}\left(\frac{\omega L I_{\rm m}[n]}{E_{\rm m}[n]}\right) = \tan^{-1}\left(\frac{\omega L\sqrt{i_{\rm dr}^2[n]+i_{\rm qr}^2[n]}}{\sqrt{e_{\rm d}^2[n]+e_{\rm q}^2[n]}}\right) \tag{21}$$

$$\varphi[n] = \tan^{-1}\left(\frac{Q[n]}{P[n]}\right) = \tan^{-1}\left(\frac{e_{\rm q}[n]\,i_{\rm dr}[n]-e_{\rm d}[n]\,i_{\rm qr}[n]}{e_{\rm d}[n]\,i_{\rm dr}[n]+e_{\rm q}[n]\,i_{\rm qr}[n]}\right) \tag{22}$$

where the effect of PF on estimating θ is neglected.

There are other ways to obtain the T_δ. For example, $I_{\rm m}$, $E_{\rm m}$, and φ can be estimated from the measured current and voltage signals by Fourier transform, least mean squares technique, and so on. In addition, if the direct power control is used, P and Q in (22) can be obtained from the reference active and reactive power. This article adopts the voltage-oriented control (VOC) from which the variables and signals required in (20)–(22) are accessible. Accordingly, T_δ can be easily estimated by these equations without complex algorithms. It should be pointed out that $I_{\rm m}$ is estimated by reference currents rather than actual currents. In the normal and stable operation, actual currents are close to their references. After OC faults occur, actual currents usually drop dramatically, while reference currents will increase due to the regulation of the current loop [37]. For this reason, using reference currents can improve thresholds to avoid misdiagnosis for successive OC faults.

In order to distinguish between inner switch faults and outer switch faults, two thresholds are designed as follows:

$$\varepsilon_{\rm a1}[n] = \begin{cases} \varepsilon_{\rm a1}[n-1] + D_{\rm a}[n-1], & \gamma_{\rm a}[n] \neq i\cdot\pi \\ k_1[n]\cdot T_\delta[n]/T_{\rm s}, & \gamma_{\rm a}[n] = i\cdot\pi \end{cases},\quad i\in\{0,\ 1\}$$

$$\varepsilon_{\rm a2}[n] = \begin{cases} \varepsilon_{\rm a2}[n-1] + D_{\rm a}[n-1], & \gamma_{\rm a}[n] \neq i\cdot\pi \\ k_2[n]\cdot T_\delta[n]/T_{\rm s}, & \gamma_{\rm a}[n] = i\cdot\pi \end{cases},\quad i\in\{0,\ 1\} \tag{23}$$

where $\varepsilon_{\rm a1}$ is the small threshold for $\Delta\bar{v}_{\rm ao\_sum}$ to diagnose the faulty pair, and $\varepsilon_{\rm a2}$ is the large threshold for $\Delta\bar{v}_{\rm ao\_sum}$ to diagnose inner switch faults of phase a. $\varepsilon_{\rm a1}$ and $\varepsilon_{\rm a2}$ are jointly used to diagnose outer switch faults of phase a. Similarly, thresholds for $\Delta\bar{v}_{\rm bo\_sum}$ and $\Delta\bar{v}_{\rm co\_sum}$ can be obtained.

If the average value of $D_{\rm Pa}$ in $R_{\rm a1}$ is d, the accumulation of $D_{\rm Pa}$ in $R_{\rm a1}$ can be estimated as $d\cdot T_\delta/T_{\rm s}$. According to Section III, d is different in the normal condition (d_1), the $S_{\rm a1}$ fault condition (d_2), and the $S_{\rm a2}$ fault condition (d_3). Accordingly, k_1 and k_2 are selected based on d_1, d_2, and d_3. When PF $= 1$, outer switch faults are not easily observable and not fatal to rectifiers. In this condition, it is more important to detect inner switch faults accurately and fast. Therefore, k_1 and k_2 can be set as the same constant. Because T_δ is small, a large value (>1) set for k_1 and k_2 provides some margin for ensuring reliability. When PF < 1, the effect of outer-switch faults expands. It is necessary to distinguish between inner switch faults and outer switch faults in this condition. The difference between $S_{\rm a1}$ fault and $S_{\rm a2}$ fault is that $S_{\rm a1}$ fault does not appreciably make $R_{\rm a1}$ extend as $S_{\rm a2}$ fault does. Since T_δ is the estimated duration of $R_{\rm a1}$ in the normal condition, the accumulated $D_{\rm Pa}$ (within longer $R_{\rm a1}$) must be larger than $T_\delta/T_{\rm s}$ after $S_{\rm a2}$ fault, and the accumulated $D_{\rm Pa}$ (within normal $R_{\rm a1}$) is usually smaller than $T_\delta/T_{\rm s}$ after $S_{\rm a1}$ fault. Therefore, k_2 can be set as a value around 1 to detect inner switch faults. For k_1, it is known that $d_1 < k_1 < d_2 < k_2$. It can be observed from Fig. 4 that d_1 is smaller than 0.5 in different operating states. In order to distinguish outer switch faults from inner switch faults, k_1 is better as much smaller than k_2 as possible. Therefore, k_1 can be set as a value around 0.5 to detect outer switch faults. However, d_1, d_2, and d_3 increase with the decrease in PF. Besides, compared with a lag angle ($\varphi < 0$), a lead angle ($\varphi > 0$) further promotes their increase. Therefore, k_1 and k_2 should be adjusted by φ. With the assistance of simulation tests, the expressions of k_1 and k_2 are defined as follows:

$$\begin{cases} k_2[n] = k_1[n] = 3, & |\varphi[n]| \le 0.1 \text{ rad} \\ k_2[n] = 2k_1[n] = \sec^2(\varphi[n]), & \varphi[n] > 0.1 \text{ rad} \\ k_2[n] = 2k_1[n] = \sec(\varphi[n]), & \varphi[n] < -0.1 \text{ rad}. \end{cases} \tag{24}$$

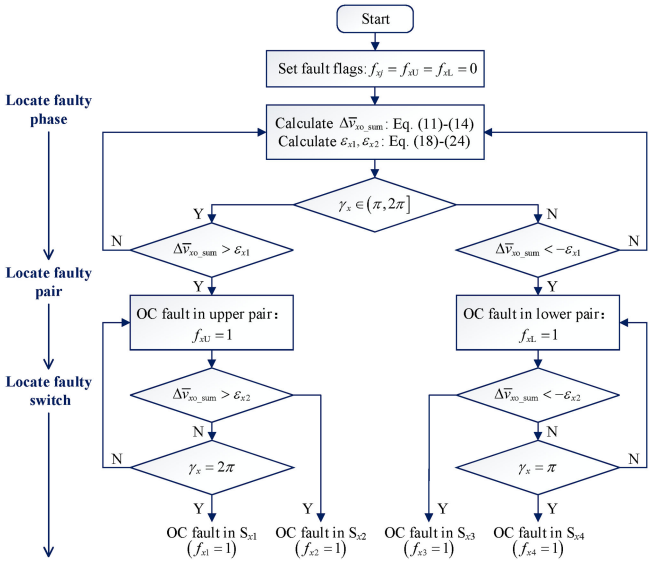

Fig. 8. Proposed fault diagnosis flow chart.

C. Fault Detection and Location

The proposed fault diagnosis flowchart is demonstrated in Fig. 8. First, diagnostic variables ($\Delta\bar{v}_{x\rm o\_sum}$) and thresholds ($\varepsilon_{x1}, \varepsilon_{x2}$) are calculated. If $\Delta\bar{v}_{x\rm o\_sum}$ crosses the small threshold $\pm\varepsilon_{x1}$ when the particular current angle condition is satisfied,

the faulty phase is detected. At the same time, the faulty pair can be determined according to the polarity of $\Delta\bar{v}_{xo\_sum}$. At present, it cannot be determined whether the inner switch or the outer switch in this pair is faulty because $\Delta\bar{v}_{xo\_sum}$ may cross the large threshold $\pm\varepsilon_{x2}$ afterward. After the faulty pair is detected, if $\Delta\bar{v}_{xo\_sum}$ crosses the large threshold $\pm\varepsilon_{x2}$ later, the inner switch fault in this faulty pair can be identified. Otherwise, if $\Delta\bar{v}_{xo\_sum}$ is always within the large threshold $\pm\varepsilon_{x2}$ before $\gamma_x = \pi$ (or $\gamma_x = 2\pi$), the outer switch fault in this faulty pair can be identified. Therefore, the detection and location of a single OC fault can be accomplished according to Fig. 8. Here, f_{xj} ($j \in \{1,\ 2,\ 3,\ 4\}$) are fault flags representing the state of switches. $f_{xj} = 0$ means that switch S_{xj} is in the healthy state and $f_{xj} = 1$ means that switch S_{xj} is in the OC state. $f_{x\mathrm{U}}$ and $f_{x\mathrm{L}}$ are fault flags representing the state of switches in a pair. $f_{x\mathrm{U}} = 0$ means that there is no OC fault in both S_{x1} and S_{x2}. $f_{x\mathrm{U}} = 1$ means that there is an OC fault at least in one of S_{x1} and S_{x2}. $f_{x\mathrm{L}} = 0$ means that there is no OC fault in both S_{x3} and S_{x4}. $f_{x\mathrm{L}} = 1$ means that there is an OC fault at least in one of S_{x3} and S_{x4}.

The proposed diagnosis method can identify inner switch faults in various operating states and detect outer switch faults if their fault characteristics are apparent enough. Under unity power factor, outer switch faults are imperceptible by the proposed diagnostic variables. Only inner switch faults can be detected because k_1 and k_2 are set as large values under unity power factor. Therefore, there is no confusion between inner switch faults and outer switch faults. Under nonunity power factor, there are similarities between inner switch faults and outer switch faults. The proposed thresholds can distinguish them. Only in the worst situation that an OC fault occurs in $\mathrm{S}_{\mathrm{a}2}$ at the end of $R_{\mathrm{a}2}$, $\mathrm{S}_{\mathrm{a}2}$ fault may be temporarily misdiagnosed as $\mathrm{S}_{\mathrm{a}1}$ fault or be missed in this current cycle because there are not enough switching periods allowing the increment in D_{Pa} to accumulate. However, $\mathrm{S}_{\mathrm{a}2}$ fault can be detected in the next current cycle. Overall, although the proposed diagnosis method cannot detect outer switch faults in all operating states, it possesses the capability of distinguishing between inner switch faults and outer switch faults.

Moreover, the proposed diagnosis method can be applied to trigger different fault-tolerant strategies. In terms of some fault-tolerant strategies, such as the redundant parallel leg solution and the dc-bus midpoint connection [39], locating the faulty phase is enough for postfault reconfiguration. The proposed method detects the faulty phase and pair before identifying the faulty switch. Hence, by removing large thresholds and the fault identification process, the proposed method can be applied to these fault-tolerant strategies with a simpler procedure and a faster detection speed. In addition, locating the faulty switch is required for some fault-tolerant strategies based on modified modulation [14], [32]–[34]. With the development of these methods, various multiple-switch faults can be compensated to a certain extent. Since the fault characteristics of each switch reflected by diagnostic variables are not changed by other concurrent OC faults, the proposed method can diagnose each OC fault in multiple-switch faults by the same procedure in Fig. 8. No additional diagnostic variables and rules are required for multiple-switch faults. Therefore, the proposed diagnosis method is simpler and more accurate in diagnosing multiple-switch faults.

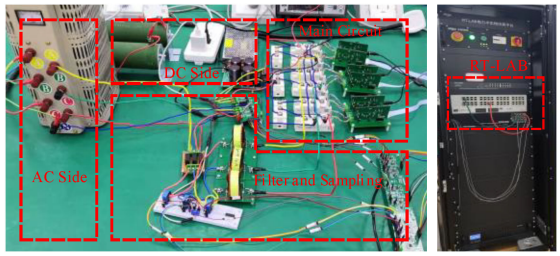

Fig. 9. Experimental platform of three-phase 3L-NPC rectifier.

In terms of multiple-switch faults, some fault combinations contribute to the diagnosis, while others bring some adverse effects, mainly reflected in the longer diagnostic time. In case of double-switch faults, there are three types of fault combinations as follows.

Type 1: Two faults are in the same pair, such as $\mathrm{S}_{\mathrm{a}1}$ fault and $\mathrm{S}_{\mathrm{a}2}$ fault. $\mathrm{S}_{\mathrm{a}2}$ fault characteristics completely cover $\mathrm{S}_{\mathrm{a}1}$ fault characteristics, and $\mathrm{S}_{\mathrm{a}1}$ fault remains undetected, which is a common feature of most existing diagnosis methods.

Type 2: Two faults are in different pairs of the same phase, such as $\mathrm{S}_{\mathrm{a}2}$ fault and $\mathrm{S}_{\mathrm{a}3}$ fault. Since $R_{\mathrm{a}2}$ and $R_{\mathrm{a}3}$ are not overlapped, the two faults usually do not affect each other.

Type 3: Two faults are in different phases. Some fault combinations promote the diagnosis, while others slow down the diagnosis. For example, $\mathrm{S}_{\mathrm{b}3}$ fault co-occurs with $\mathrm{S}_{\mathrm{a}2}$ fault when i_{a} goes into the negative half-cycle. As mentioned before, $\mathrm{S}_{\mathrm{a}2}$ fault makes an inverse rotation of the reference voltage vector $\boldsymbol{V}$ from Sector II to Sector I. Under the effect of $\mathrm{S}_{\mathrm{b}3}$ fault, $\boldsymbol{V}$ will rotate backward more seriously even to Sector V and Sector VI. This is because $\mathrm{S}_{\mathrm{b}3}$ fault makes an inverse rotation of $\boldsymbol{V}$ from Sector I to Sector VI at this time. Then, $R_{\mathrm{a}1}$ extends more heavily compared with the $\mathrm{S}_{\mathrm{a}2}$ single-fault condition. Accordingly, $\Delta\bar{v}_{\mathrm{ao\_sum}}$ increases faster and reaches a larger peak, which is helpful to diagnose $\mathrm{S}_{\mathrm{a}2}$ fault. On the contrary, $\mathrm{S}_{\mathrm{b}2}$ fault hinders the inverse rotation of $\boldsymbol{V}$ from Sector II to Sector I caused by $\mathrm{S}_{\mathrm{a}2}$ fault, making $R_{\mathrm{a}1}$ shorter than that in the $\mathrm{S}_{\mathrm{a}2}$ single-fault condition. Accordingly, the diagnostic time of $\mathrm{S}_{\mathrm{a}2}$ fault increases.

A similar analysis can be conducted for other double OC faults and three or more OC faults. For example, three OC faults co-occur in $\mathrm{S}_{\mathrm{a}2}$, $\mathrm{S}_{\mathrm{b}2}$, and $\mathrm{S}_{\mathrm{b}3}$. The effect of the other two faults on diagnosing $\mathrm{S}_{\mathrm{a}2}$ fault can be analyzed separately as the cases of double-switch faults. That is, $\mathrm{S}_{\mathrm{b}2}$ fault may bring out negative effects, and $\mathrm{S}_{\mathrm{b}3}$ fault may bring out positive effects.

V. Experimental Results

A. Experimental Setup

Experiments have been performed on a three-phase 3L-NPC rectifier platform, as shown in Fig. 9. The main experimental parameters are listed in Table I. The rectifier consists of insulated-gate bipolar transistors (IGBTs). The control of the system and the proposed diagnosis method are implemented

TABLE I
EXPERIMENTAL PARAMETERS

Parameter	Symbol	Value
Grid phase voltages	e_a , e_b , e_c	50 V (rms), 50 Hz
Given dc bus voltage	V	130 V
Load	R_L	100 Ω
Capacitance	C	940 μF
Filter inductance	L	5 mH
Switching/Sampling frequency	f_s	10 kHz

by a real-time laboratory (RT-LAB) test platform OP5700. To better demonstrate the experimental results, all data obtained by the RT-LAB platform are saved and imported into MATLAB for replotting. In the following tests, OC faults of IGBTs are simulated by disabling the related gate signals. In the following experimental figures, the undrawn fault flags mean that the values of these flags are always zero. The current threshold (h) is set as 0.1 A (about 5% of I_m).

B. Experiment I: Diagnostic Performance

Figs. 10 and 11 confirm the validity of the proposed diagnosis method applied to multiple-switch faults under unity power factor with different I_m and M. Since $\varepsilon_{x1} = \varepsilon_{x2}$, only ε_{x2} is plotted. In Fig. 10, M is large (about 0.95) and I_m is small. After S_{a1} fault occurs, i_a is hardly distorted, and $\Delta\bar{v}_{ao\_sum}$ is within $\pm\varepsilon_{a2}$ as normal, which indicates outer switch faults cannot be detected. Then, S_{a2}, S_{b2}, and S_{c3} faults co-occur at the beginning of R_{a2}. At first, i_a is distorted with zero sections, and $\Delta\bar{v}_{ao\_sum}$ has an accelerated tendency to increase and cross ε_{a2}, indicating S_{a2} fault. After i_c goes into the positive half-cycle, where S_{c3} is in its working range (R_{c3}), $\Delta\bar{v}_{co\_sum}$ has an accelerated tendency to decrease and cross $-\varepsilon_{c2}$, indicating S_{c3} fault. After i_b goes into the negative half-cycle, where S_{b2} is in its working range (R_{b2}), three OC faults simultaneously affect the system performance. An accelerated increase in $\Delta\bar{v}_{bo\_sum}$ makes it cross ε_{b2}, which refers to S_{b2} fault. The experiment in Fig. 11 was conducted under the given dc bus voltage of 160 V with increased load power. Compared with Fig. 10, M decreases (about 0.75) and I_m increases in Fig. 11. In the normal condition, the maximum value and the growth rate of diagnostic variables in Fig. 11 are larger than those in Fig. 10 due to the higher duty cycle of the switching state [O], which is the basis for thresholds. The variation in I_m and M causing the increase in the duty cycle of the switching state [P] (or [N]) is taken into account in the threshold setting as well. Benefit from those, thresholds in Fig. 11 are self-adjustable to fit the system operating state without any manual modification, ensuring that diagnostic variables are within thresholds in the normal condition. Multiple inner-switch faults such as S_{a2}, S_{b3}, and S_{c2} faults are accurately detected in Fig. 11. However, S_{a1} fault still cannot be observed.

Figs. 12 and 13 confirm the validity of the proposed diagnosis method applied to multiple-switch faults under nonunity power factor. In the normal condition of Fig. 12 ($\varphi > 0$), diagnostic variables increase or decrease at a fast speed at the beginning of a half current cycle and then slowly reach the maximum or

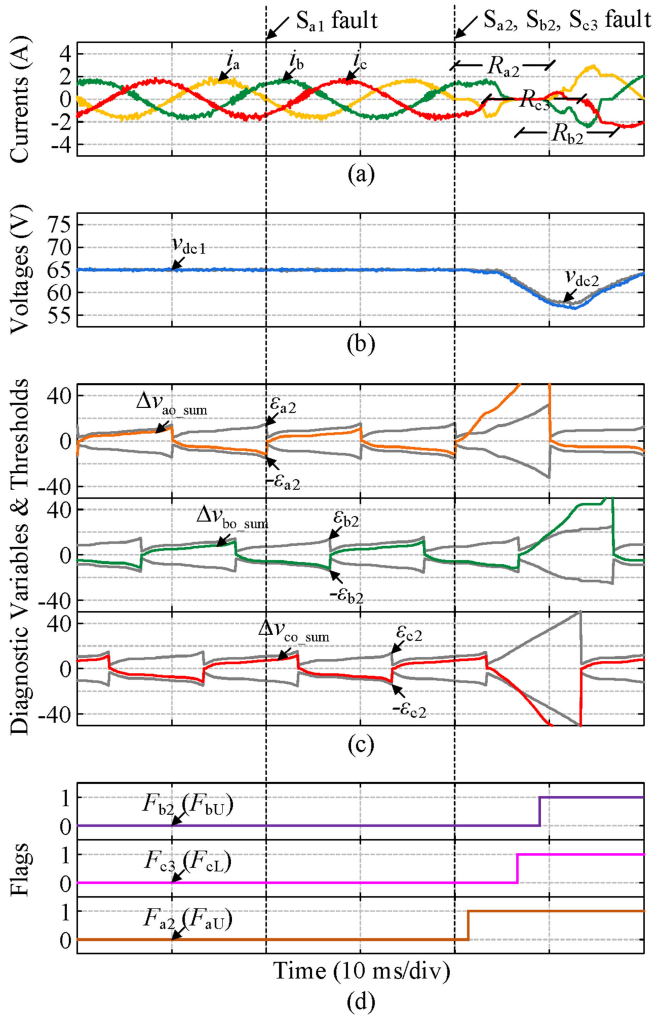

Fig. 10. Experimental results in case of S_{a1}, S_{a2}, S_{b2}, and S_{c3} faults when $PF = 1$ with small I_m and large M. (a) Currents. (b) Capacitor voltages. (c) Diagnostic variables and thresholds. (d) Fault flags.

minimum. After S_{a1} fault occurs, i_a is distorted with Z1. At first, $\Delta\bar{v}_{ao\_sum}$ increases faster and crosses ε_{a1}. Accordingly, the faulty switch can be located in the upper pair of phase a ($f_{aU} = 1$). After that, $\Delta\bar{v}_{ao\_sum}$ remains below ε_{a2} in the half-cycle, which refers to S_{a1} fault. Then, S_{a2} and S_{b3} faults occur at the same time. For both faults, the corresponding phase diagnostic variable crosses the small threshold first, and the faulty pair is determined before the faulty switch is identified. After that, the diagnostic variable continuously increases or decreases at a fast speed and crosses the large threshold, which refers to the inner switch fault in the faulty pair. The experiment in Fig. 13 was carried out when $\varphi < 0$. Unlike Fig. 12, diagnostic variables in Fig. 13 increase or decrease at a slow speed at the beginning of a half current cycle and then quickly reach the maximum or minimum. After S_{a1} fault occurs, i_a is distorted with Z2. In Z2, $\Delta\bar{v}_{ao\_sum}$ increases faster and crosses ε_{a1} but does not surpass ε_{a2} before the end of this half-cycle, which implies S_{a1} fault. Then, S_{a2} and S_{c3} faults co-occur and are identified accurately after the faulty pair is determined. However, the diagnostic speed of S_{a2} fault in Fig. 13 is much longer than that in Fig. 12. This is because

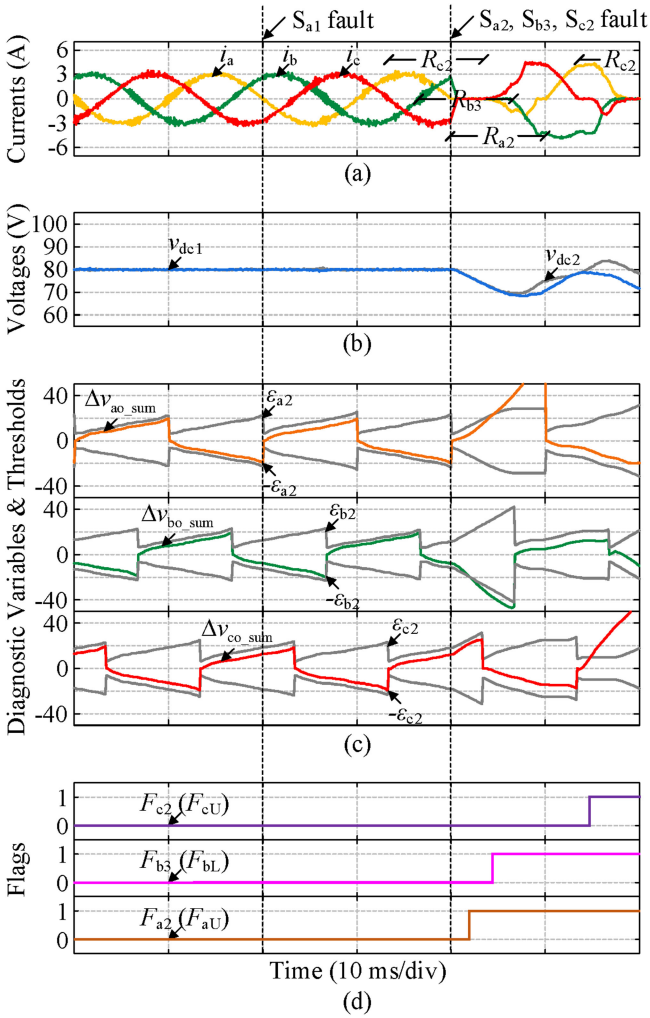

Fig. 11. Experimental results in case of S_{a1}, S_{a2}, S_{b3}, and S_{c2} faults when $PF = 1$ with large I_m and small M. (a) Currents. (b) Capacitor voltages. (c) Diagnostic variables and thresholds. (d) Fault flags.

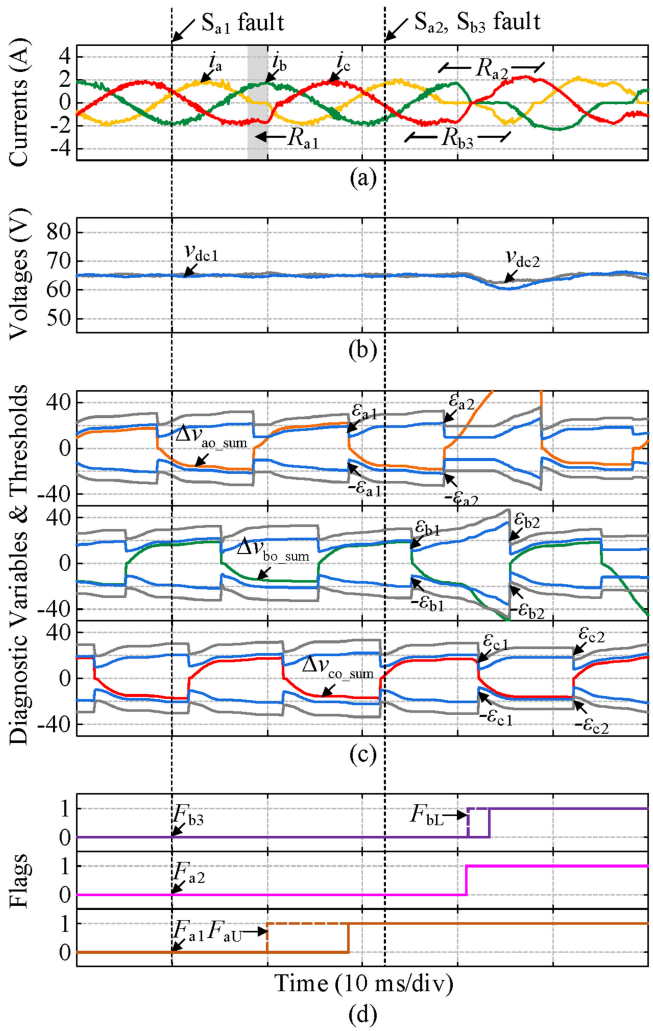

Fig. 12. Experimental results in case of S_{a1}, S_{a2}, and S_{b3} faults when PF < 1 ($\varphi > 0$). (a) Currents. (b) Capacitor voltages. (c) Diagnostic variables and thresholds. (d) Fault flags.

R_{a1} of Fig. 12 mainly extends in Z1, making $\Delta\bar{v}_{ao\_sum}$ steeply increase in Z1 (where S_{a2} fault starts), while R_{a1} of Fig. 13 mainly extends in Z2, making $\Delta\bar{v}_{ao\_sum}$ steeply increase in Z2 (which is away from S_{a2} fault onset).

The experimental results in Figs. 10–13 confirm the analysis in Section III and prove that the proposed diagnosis method is valid for multiple-switch faults of NPC rectifiers in various operating states. Besides, the proposed diagnosis method shows robustness against voltage imbalance. It can be seen from Figs. 10–13 that the upper and lower capacitor voltages are unbalanced after OC faults occur. The proposed diagnostic variables use the actual upper and lower capacitor voltages for calculation, and the threshold setting is improved by incorporating the voltage imbalance factor. These procedures make the diagnosis method immune to voltage imbalance. Generally, the proposed method presents a good performance in the diagnostic speed and accuracy of inner switch faults. Outer switch faults are perceptible under nonunity power factor, and they can be detected and distinguished from inner switch faults by the proposed method. It takes quite a long time to locate outer switch faults. However, before the outer switch fault is identified, its pair can be detected quickly. If the fault-tolerant control and the maintenance only require the information of the faulty pair, the proposed method can provide an instant diagnostic result.

C. Experiment II: Robustness Performance

Figs. 14 and 15 evaluate the robustness of the proposed diagnosis method against dc and ac side disturbances. Since ε_{x1} is more sensitive to OC faults, only ε_{x1} is plotted. The experimental results in Fig. 14 prove that the proposed adaptive thresholds make diagnosis more robust against the dc bus voltage and load power variation. As indicated in Fig. 14(c), adaptive thresholds are more sensitive to current variation than diagnostic variables because they are estimated by reference currents. In this way, adaptive thresholds effectively guarantee diagnostic robustness during the load variation. However, the response of nonadaptive thresholds to the current variation is insensitive. For nonadaptive thresholds, $k_1 \cdot T_\delta/T_s$ and $k_2 \cdot T_\delta/T_s$ in (23) are set as predefined constants. If I_m increases, nonadaptive thresholds

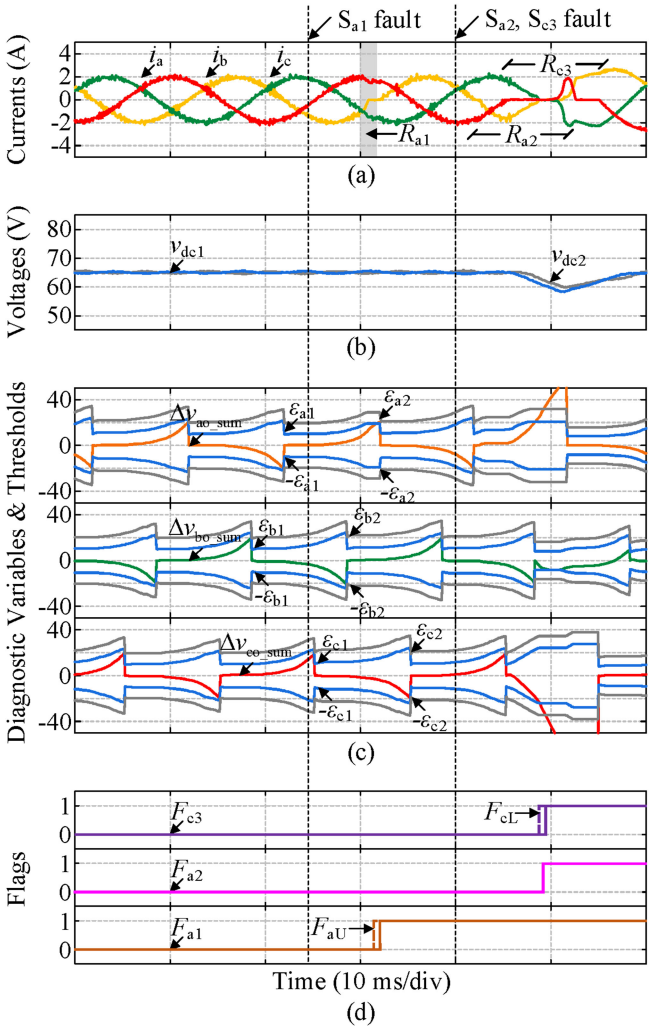

Fig. 13. Experimental results in case of S_{a1}, S_{a2}, and S_{c3} faults when PF < 1 ($\varphi < 0$). (a) Currents. (b) Capacitor voltages. (c) Diagnostic variables and thresholds. (d) Fault flags.

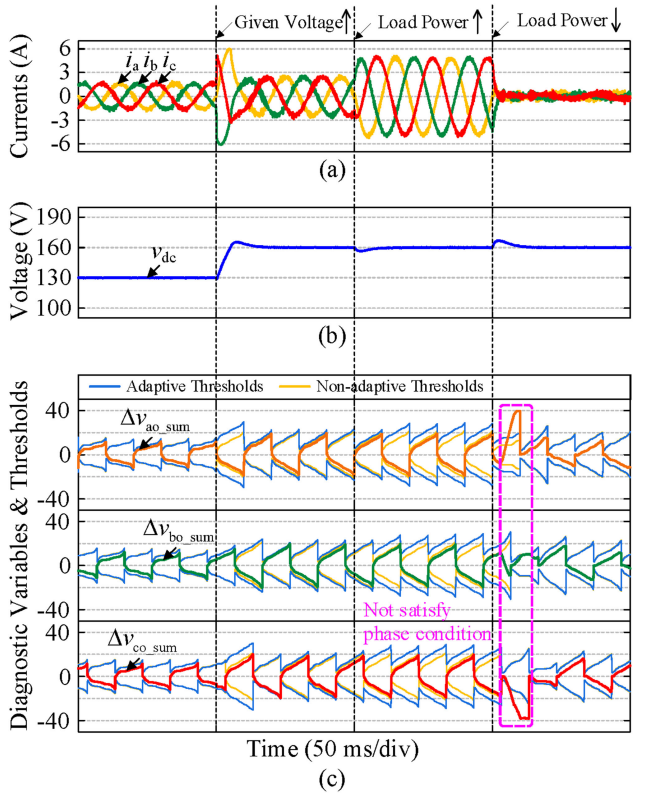

Fig. 14. Experimental results under load variation. (a) Currents. (b) DC bus voltage. (c) Diagnostic variables and thresholds.

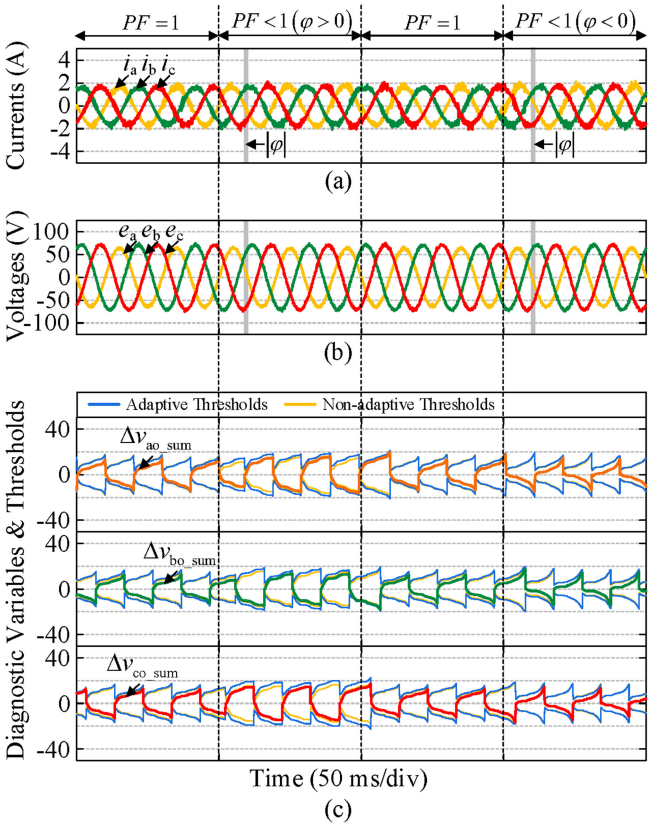

Fig. 15. Experimental results under ac side imbalance and power factor variation. (a) Currents. (b) Grid voltages. (c) Diagnostic variables and thresholds.

are close to or even below the diagnostic variables, leading to misdiagnosis. $k_1 \cdot T_\delta/T_s$ and $k_2 \cdot T_\delta/T_s$ can be set as larger values to prevent misdiagnosis in the large-current condition, but the diagnosis may take more time when I_m decreases. With the unbalanced grid voltages ($e_a = 45$ Vrms, $e_b = e_c = 50$ Vrms), the experiment in Fig. 15 shows that adaptive thresholds vary with PF, and no diagnostic variables cross adaptive thresholds in the normal condition. On the contrary, diagnostic variables might cross non-adaptive thresholds when PF < 1 (especially when $\varphi > 0$), resulting in misdiagnosis. Experimental results verify that the proposed adaptive thresholds make the diagnosis robust against the grid voltage imbalance and the power factor variation. Besides, since adaptive thresholds require the inductance value obtained from the control loop, it is necessary to assess the effect of the inductance error. In Fig. 15, 20% of the parameter error relative to the actual inductance ($L'_a = 0.8L_a$, $L'_b = 1.2L_b$, $L'_c = 1.2L_c$) is introduced to calculate adaptive thresholds. No misdiagnosis happens. k_1 and k_2 in (24) can be adjusted to achieve higher reliability by taking the inductance error into account because the inductance error is approximately linear

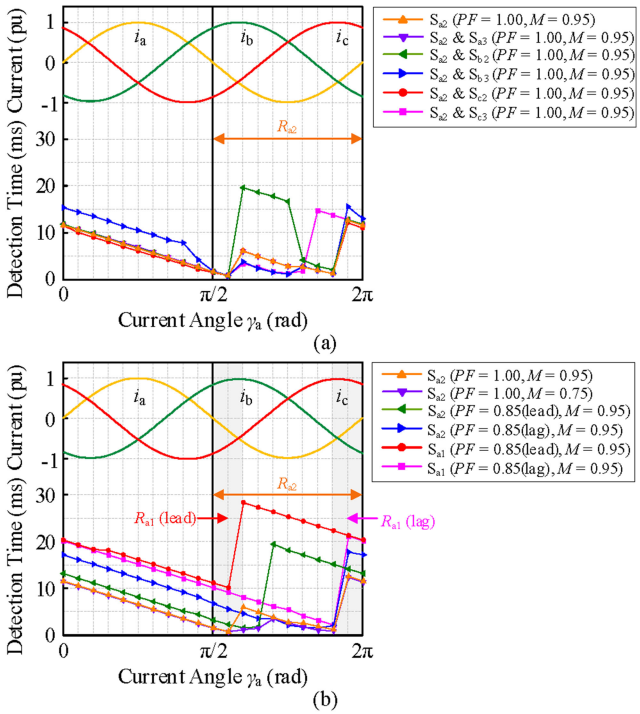

Fig. 16. Detection time. (a) S_{a2} fault with other faults under unity power factor. (b) S_{a1} fault and S_{a2} fault in different operating conditions.

with the predicted value of T_δ/T_s. For example, if 20% of the reduction in the inductance value is considered, increasing k_1 and k_2 by 20% can offset this error.

The experimental results in Figs. 14 and 15 confirm the contribution of the proposed adaptive thresholds to diagnostic robustness in various operating states of NPC rectifiers.

D. Detection Time

Fig. 16 presents the detection time of S_{a1} fault and S_{a2} fault occurring at different times in a current cycle. The main factor affecting the detection speed is the fault occurrence time. If S_{a2} fault occurs within R_{a2}, the diagnosis can be completed as fast as several switching periods. If S_{a2} fault occurs out of R_{a2}, the diagnosis is delayed to the next half-cycle, which is a common feature of the existing fault diagnosis methods. Other inner switch faults co-occurring with S_{a2} fault also affect the detection speed of S_{a2} fault, as shown in Fig. 16(a). When S_{a2} fault occurs within R_{a2}, simultaneous S_{b2} fault slows the detection speed of S_{a2} fault, whereas simultaneous S_{b3} fault speeds up the diagnosis of S_{a2} fault, which confirms the theoretical analysis in Section IV-C. Fig. 16(b) shows the detection time of S_{a1} fault and S_{a2} fault in different operating states of NPC rectifiers. Since outer switch faults can be determined only at the end of each half current cycle, the detection time of S_{a1} fault presents a linear relationship with the fault occurrence time and reaches the minimum when the fault occurs within R_{a1}. Generally, the proposed diagnosis method shows a better performance in the detection speed under unity power factor, and the average detection time in a current cycle is longer under nonunity power factor.

E. Comparison With Other Relevant Methods

Table II gives a comparison between the proposed method and relevant methods, mainly in terms of diagnostic capability, time, and robustness.

1) *Diagnostic Capability:* Most diagnosis methods for NPC converters only consider single-switch faults. A voltage-based method proposed in [19] can detect multiple-switch faults of NPC converters efficiently and quickly by using extra hardware, along with the increase in cost and space. A model-based method proposed in [25] can detect multiple-switch faults of two-level inverters by designing new diagnostic rules for each fault combination. Multiple-switch faults are more complicated as the number of switches increases. Thereby, using this method to diagnose multiple-switch faults of NPC converters will heavily increase the diagnostic complexity and unreliability. Besides, it is challenging to set thresholds for distinguishing between inner switch faults and outer switch faults. In comparison, the proposed method has advantages in diagnosing multiple-switch faults of NPC rectifiers without complex diagnostic rules.
2) *Diagnostic Time:* It should be mentioned that only the diagnostic time of inner switch faults is considered for NPC converters in Table II. In most cases, current-based methods require a long diagnostic time, such as the normalized average current-based method in [12]. Voltage-based methods usually show an outstanding performance in diagnostic speed since these methods utilize extra measurable signals (such as terminal voltages, which are only accessible from a single-phase 5L-NPC inverter in [18]) or extra hardware (such as three voltage sensors in [19]). Accordingly, the improvement in diagnostic speed is at the expense of limited application or increased cost. Although the diagnostic speed of the proposed method may not be as fast as the voltage-based method [18], [19], it is a cost-effective method and generally faster than current-based methods [11], [12].
3) *Diagnostic Accuracy and Robustness:* Current-based methods, such as the method in [11], are usually affected by load variations and perform poorly in the low-current condition. Model-based methods, such as the method in [26], are highly dependent on precise modeling, and the modeling error will affect diagnostic accuracy. Methods in [18], [19], and [26] rely on a high sampling frequency (at least higher than the switching frequency) to realize fast and accurate identification. This requirement increases the software burden and makes those methods difficult to be applied in high switching frequency systems. The accuracy and robustness can be improved by normalizing diagnostic variables (such as the method in [12]) or by designing adaptive thresholds (such as the method in [25]). In addition to using adaptive thresholds, the proposed method considers several factors that affect postfault characteristics, such as current amplitude, modulation index, and power factor, which are not discussed in most diagnosis methods. Therefore, the proposed method can be applied

TABLE II
COMPARISON WITH RELEVANT METHODS

Relevant method	Diagnostic variable	Detected fault type	Extra sensor	Longest diagnostic time (within the switch working range)	Robustness	Application
[11]	Duration of zero current	Single-switch faults	No	Medium (Within a half of the fundamental period)	Low	3L-NPC back-to-back convert
[12]	Average current	Single-switch faults	No	Long (At least two fundamental periods)	Medium	3L-NPC inverter
[18]	Terminal voltage	Single-switch faults	No	Short (Several sampling periods)	High	Single-phase 5L-NPC inverter
[19]	Measured pole voltage	Multiple-switch faults	Yes	Short (Several sampling periods)	High	3L-NPC inverter
[25]	Average phase-to-phase pole voltage deviation	Multiple-switch faults	No	Short (Several switching periods)	High	2L-VSC inverter
[26]	Instant phase-to-phase pole voltage deviation	Single-switch faults	No	Medium (Within 15% of the fundamental period)	Medium	3L-NPC rectifier
Proposed	Phase pole voltage deviation based on fault assumption	Multiple-switch faults	No	Medium (Within a quarter of the fundamental period)	High	3L-NPC rectifier

to various operating states of NPC rectifiers with high robustness.

Overall, the proposed method has a good comprehensive diagnostic performance. It makes a good tradeoff between the speed and the cost. Also, it has merits of high diagnostic capability and high robustness with low sampling requirement and low dependence on precise modeling.

VI. CONCLUSION

This article proposes a new OC fault diagnosis method in 3L-NPC rectifiers. The accumulations of three-phase average voltage deviations in a half current cycle are utilized as the diagnostic variables. The average voltage deviations are the differences between average switching-state-based voltages and average fault-assumed-based voltages, which are obtained without extra hardware and precise modeling. The diagnostic variables are not zero in the normal condition, and they have an accelerated tendency to increase (or decrease) after OC faults because of a more extended range and increased duty cycle of the switching state [P] (or [N]), providing a basis for diagnosis. Besides, adaptive thresholds are proposed by considering various factors that may affect the diagnostic performance, such as the voltage imbalance, the current amplitude, the modulation index, and the power factor. In this way, the proposed method has the adaptability to different operating states of NPC rectifiers and possesses stronger robustness against transient changes. Compared with relevant model-based methods using voltage deviations, the proposed method is less dependent on modeling and accessible to detect multiple-switch faults more accurately and simply. The effectiveness and robustness of the proposed method have been verified by experimental results. Also, the detection time of different fault combinations occurring at different times is tested in various operating states. Given that no additional sensors are used, the proposed method possesses rapidity in diagnosing inner-switch faults. Outer switch faults can be detected under nonunity power factor with a relatively long diagnostic time. Further study can be conducted to explore the possibility of outer switch fault diagnosis under unity power factor and improve the diagnostic speed of outer switch faults.

APPENDIX

When $I_{\mathrm{a}} = 0$, the expression for the voltage deviation is derived in detail here. $\mathrm{S_{a2}}$ open-circuit fault is taken as an example for analysis.

The average modeling of the NPC rectifier is expressed as follows:

$$E_x = RI_x + L\frac{dI_x}{dt} + V_{x\mathrm{o}} + V_{\mathrm{on}}, \quad x \in \{\mathrm{a}, \mathrm{b}, \mathrm{c}\}. \tag{25}$$

For a well-performed double-closed loop controller, its output reference voltage is approximated as follows:

$$V_{x\mathrm{o}} = \bar{v}_{x\mathrm{o}} = \bar{s}_x \cdot \frac{V_{\mathrm{dc}}}{2}. \tag{26}$$

By substituting (26) into (25) and considering that $E_{\mathrm{a}} + E_{\mathrm{b}} + E_{\mathrm{c}} = 0$ and $I_{\mathrm{a}} + I_{\mathrm{b}} + I_{\mathrm{c}} = 0$ in a three-phase symmetrical system, it has

$$V_{\mathrm{on}} = -\left(\bar{s}_{\mathrm{a}} + \bar{s}_{\mathrm{b}} + \bar{s}_{\mathrm{c}}\right) \cdot \frac{V_{\mathrm{dc}}}{6}. \tag{27}$$

By substituting (27) into (25) and ignoring the resistance term, a-phase current rate of change can be calculated as follows:

$$L\frac{dI_{\mathrm{a}}}{dt} = E_{\mathrm{a}} - \left(\frac{\bar{s}_{\mathrm{a}}}{3} - \frac{\bar{s}_{\mathrm{b}}}{6} - \frac{\bar{s}_{\mathrm{c}}}{6}\right) \cdot V_{\mathrm{dc}}. \tag{28}$$

By substituting (2) and (26) into (7), the voltage deviation when $I_{\mathrm{a}} = 0$ can be written as follows:

$$\Delta\bar{v}_{\mathrm{ao}} = \frac{1}{2}\left(2V_{\mathrm{ao}} - V_{\mathrm{bo}} - V_{\mathrm{co}} - 3E_{\mathrm{a}}\right). \tag{29}$$

For a three-phase symmetrical rectifier system, the reference voltages satisfy the following equations:

$$\begin{cases} V_{\mathrm{an}} + V_{\mathrm{bn}} + V_{\mathrm{cn}} = 0 \\ V_{\mathrm{ao}} - V_{\mathrm{bo}} = V_{\mathrm{an}} - V_{\mathrm{bn}} \\ V_{\mathrm{ao}} - V_{\mathrm{co}} = V_{\mathrm{an}} - V_{\mathrm{cn}}. \end{cases} \tag{30}$$

According to (30), (29) is transformed as follows:

$$\Delta\bar{v}_{\mathrm{ao}} = \frac{3}{2}\left(V_{\mathrm{an}} - E_{\mathrm{a}}\right). \tag{31}$$

TABLE III
EFFECT OF VOLTAGE VECTORS ON CURRENT RATE OF CHANGE

V_i	k_{V_i}	V_i	k_{V_i}
V_1 (POO/ONN)	1/3	V_4 (OPP/NOO)	-1/3
V_2 (PPO/OON)	1/6	V_3 (OPO/NON)	-1/6
V_6 (POP/ONO)	1/6	V_5 (OOP/NNO)	-1/6
V_{13} (PNN)	2/3	V_{16} (NPP)	-2/3
V_{14} (PPN)	1/3	V_{15} (NPN)	-1/3
V_{18} (PNP)	1/3	V_{17} (NNP)	-1/3
V_7 (PON)	1/2	V_9 (NPO)	-1/2
V_{12} (PNO)	1/2	V_{10} (NOP)	-1/2
V_8 (OPN)	0	V_{11} (ONP)	0

According to (25), and ignoring the resistance term, (31) is further expressed as follows:

$$\Delta\bar{v}_{\mathrm{ao}} = -\frac{3}{2}\cdot L\frac{dI_{\mathrm{a}}}{dt}. \tag{32}$$

By substituting (28) into (32), the voltage deviation when $I_{\mathrm{a}} = 0$ is modified as follows:

$$\Delta\bar{v}_{\mathrm{ao}} = -\frac{3}{2}\left[E_{\mathrm{a}} - \left(\frac{\bar{s}_{\mathrm{a}}}{3} - \frac{\bar{s}_{\mathrm{b}}}{6} - \frac{\bar{s}_{\mathrm{c}}}{6}\right)\cdot V_{\mathrm{dc}}\right]. \tag{33}$$

In the SVPWM method, $\Delta\bar{v}_{\mathrm{ao}}$ in (33) can be rewritten as follows:

$$\Delta\bar{v}_{\mathrm{ao}} = -\frac{3}{2}\left(E_{\mathrm{a}} - \frac{V_{\mathrm{dc}}}{T_s}\sum k_{V_i}t_{V_i}\right) \tag{34}$$

where $k_{V_i} = (2s_{\mathrm{a}} - s_{\mathrm{b}} - s_{\mathrm{c}})/6$, and k_{V_i} can reflect the effect of the voltage vector on the current rate of change. t_{V_i} is the working time of the corresponding voltage vector in a switching period ($\sum t_{V_i} = T_{\mathrm{s}}$). Eighteen nonzero voltage vectors $\boldsymbol{V}_i$ ($i = 1, 2, \ldots, 18$) with diverse magnitudes and angles constitute the voltage space vector diagram, as depicted in Fig. 6. Four of them form a seven-step switching sequence in a switching period, and they are used to calculate $\Delta\bar{v}_{\mathrm{ao}}$ in (34). Table III lists all expressions for k_{V_i}. Therefore, when $I_{\mathrm{a}} = 0$, $\Delta\bar{v}_{\mathrm{ao}}$ depends on the grid voltage and the average voltage vectors applied in a switching period.

REFERENCES

[1] L. G. Franquelo, J. Rodríguez, J. I. Leon, S. Kouro, R. Portillo, and M. A. M. Prats, "The age of multilevel converters arrives," *IEEE Ind. Electron. Mag.*, vol. 2, no. 2, pp. 28–39, Jun. 2008.

[2] A. Nabae, I. Takahashi, and H. Akagi, "A new neutral-point-clamped PWM inverter," *IEEE Trans. Ind. Appl.*, vol. IA-17, no. 5, pp. 518–523, Sep. 1981.

[3] J. Rodriguez, S. Bernet, P. K. Steimer, and I. E. Lizama, "A survey on neutral-point-clamped inverters," *IEEE Trans. Ind. Electron.*, vol. 57, no. 7, pp. 2219–2230, Jul. 2010.

[4] F. Blaabjerg, M. Liserre, and K. Ma, "Power electronics converters for wind turbine systems," *IEEE Trans. Ind. Electron.*, vol. 48, no. 2, pp. 708–719, Mar./Apr. 2012.

[5] P. Lezana, J. Pou, T. A. Meynard, J. Rodriguez, S. Ceballos, and F. Richardeau, "Survey on fault operation on multilevel inverters," *IEEE Trans. Ind. Electron.*, vol. 57, no. 7, pp. 2207–2218, Jul. 2010.

[6] R. Wu, F. Blaabjerg, H. Wang, M. Liserre, and F. Iannuzzo, "Catastrophic failure and fault-tolerant design of IGBT power electronic converters–An overview," in *Proc. 39th Annu. Conf. IEEE Ind. Electron. Soc.*, 2013, pp. 507–513.

[7] R. Peuget, S. Courtine, and J. P. Rognon, "Fault detection and isolation on a PWM inverter by knowledge-based model," *IEEE Trans. Ind. Electron.*, vol. 34, no. 6, pp. 1318–1326, Sep./Oct. 1998.

[8] H. Yan, Y. Xu, F. Cai, H. Zhang, W. Zhao, and C. Gerada, "PWM-VSI fault diagnosis for a PMSM drive based on the fuzzy logic approach," *IEEE Trans. Power Electron.*, vol. 34, no. 1, pp. 759–768, Jan. 2019.

[9] S. Xu, S. Tao, W. Zheng, Y. Chai, M. Ma, and L. Ding, "Multiple open-circuit fault diagnosis for back-to-back converter of PMSG wind generation system based on instantaneous amplitude estimation," *IEEE Trans. Instrum. Meas.*, vol. 70, Mar. 2021, Art. no. 3512413, doi: 10.1109/TIM.2021.3062683.

[10] M. N. Soares, Y. Mollet, M. Kinnaert, J. Gyselinck, and J. Helsen, "Multiphysical time- and frequency-domain fault detection and isolation technique for power-electronic converters in DFIG wind turbines," *IEEE Trans. Power Electron.*, vol. 36, no. 4, pp. 3793–3802, Apr. 2021.

[11] J. S. Lee, K. B. Lee, and F. Blaabjerg, "Open-switch fault detection method of a back-to-back converter using NPC topology for wind turbine systems," *IEEE Trans. Ind. Electron.*, vol. 51, no. 1, pp. 325–335, Jan. 2015.

[12] U. M. Choi, J. S. Lee, F. Blaabjerg, and K. B. Lee, "Open-circuit fault diagnosis and fault-tolerant control for a grid-connected NPC inverter," *IEEE Trans. Power Electron.*, vol. 31, no. 10, pp. 7234–7247, Oct. 2016.

[13] A. Kersten *et al.*, "Fault detection and localization for limp home functionality of three-level NPC inverters with connected neutral point for electric vehicles," *IEEE Trans. Transp. Electrific.*, vol. 5, no. 2, pp. 416–432, Jun. 2019.

[14] J. S. Lee and K. B. Lee, "Open-switch fault tolerance control for a three-level NPC/T-type rectifier in wind turbine systems," *IEEE Trans. Ind. Electron.*, vol. 62, no. 2, pp. 1012–1021, Feb. 2015.

[15] J. Lee and K. Lee, "Open-circuit fault-tolerant control for outer switches of three-level rectifiers in wind turbine systems," *IEEE Trans. Power Electron.*, vol. 31, no. 5, pp. 3806–3815, May 2016.

[16] R. L. de Araujo Ribeiro, C. B. Jacobina, E. R. C. da Silva, and A. M. N. Lima, "Fault detection of open-switch damage in voltage-fed PWM motor drive systems," *IEEE Trans. Power Electron.*, vol. 18, no. 2, pp. 587–593, Mar. 2003.

[17] P. Fazio, G. Maragliano, M. Marchesoni, and G. Parodi, "A new fault detection method for NPC converters," in *Proc. 14th Eur. Conf. Power Electron. Appl.*, 2011, pp. 1–10.

[18] S. Ahmadi, P. Poure, S. Saadate, and D. A. Khaburi, "A real-time fault diagnosis for neutral-point-clamped inverters based on failure-mode algorithm," *IEEE Trans. Ind. Informat.*, vol. 17, no. 2, pp. 1100–1110, Feb. 2021.

[19] M. B. Abadi, A. M. S. Mendes, and S. M. Â. Cruz, "Method to diagnose open-circuit faults in active power switches and clamp-diodes of three-level neutral-point clamped inverters," *IET Elect. Power Appl.*, vol. 10, no. 7, pp. 623–632, Aug. 2016.

[20] T. Peng *et al.*, "A uniform modeling method based on open-circuit faults analysis for NPC-three-level converter," *IEEE Trans. Circuits Syst. II: Exp. Briefs*, vol. 66, no. 3, pp. 457–461, Mar. 2019.

[21] X. Zhou, J. Sun, P. Cui, Y. Lu, M. Lu, and Y. Yu, "A fast and robust open-switch fault diagnosis method for variable-speed PMSM system," *IEEE Trans. Power Electron.*, vol. 36, no. 3, pp. 2598–2610, Mar. 2021.

[22] X. Ge, J. Pu, B. Gou, and Y. Liu, "An open-circuit fault diagnosis approach for single-phase three-level neutral-point-clamped converters," *IEEE Trans. Power Electron.*, vol. 33, no. 3, pp. 2559–2570, Mar. 2018.

[23] S. M. Jung, J. S. Park, H. W. Kim, K. Y. Cho, and M. J. Youn, "An MRAS-based diagnosis of open-circuit fault in PWM voltage-source inverters for PM synchronous motor drive systems," *IEEE Trans. Power Electron.*, vol. 28, no. 5, pp. 2514–2526, May 2013.

[24] D. Zhou and Y. Tang, "A model predictive control-based open-circuit fault diagnosis and tolerant scheme of three-phase AC-DC rectifiers," *IEEE J. Emerg. Sel. Topics Power Electron.*, vol. 7, no. 4, pp. 2158–2169, Dec. 2019.

[25] Z. Li, H. Ma, Z. Bai, Y. Wang, and B. Wang, "Fast transistor open-circuit faults diagnosis in grid-tied three-phase VSIs based on average bridge arm pole-to-pole voltages and error-adaptive thresholds," *IEEE Trans. Power Electron.*, vol. 33, no. 9, pp. 8040–8051, Sep. 2018.

[26] L. M. A. Caseiro and A. M. S. Mendes, "Real-time IGBT open-circuit fault diagnosis in three-level neutral-point-clamped voltage-source rectifiers based on instant voltage error," *IEEE Trans. Ind. Electron.*, vol. 62, no. 3, pp. 1669–1678, Mar. 2015.

[27] H. Zhao and L. Cheng, "Open-switch fault-diagnostic method for back-to-back converters of a doubly fed wind power generation system," *IEEE Trans. Power Electron.*, vol. 33, no. 4, pp. 3452–3461, Apr. 2018.

[28] I. Jlassi and A. J. M. Cardoso, "A single method for multiple IGBT, current, and speed sensor faults diagnosis in regenerative PMSM drives," *IEEE J. Emerg. Sel. Topics Power Electron.*, vol. 8, no. 3, pp. 2583–2599, Sep. 2020.
[29] R. Maamouri, M. Trabelsi, M. Boussak, and F. M'Sahli, "Mixed model-based and signal-based approach for open-switches fault diagnostic in sensorless speed vector controlled induction motor drive using sliding mode observer," *IET Power Electron,* vol. 12, no. 5, pp. 1149–1159, May 2019.
[30] Y. Cheng, Y. Sun, X. Li, H. Dan, J. Lin, and M. Su, "Active common-mode voltage-based open-switch fault diagnosis of inverters in IM-drive systems," *IEEE Trans. Ind. Electron.*, vol. 68, no. 1, pp. 103–115, Jan. 2021.
[31] C. Sui, Y. He, Z. Li, and M. Chen, "The post-fault current model of voltage source converter and its application in fault diagnosis," *IEEE Trans. Power Electron.*, vol. 36, no. 2, pp. 1209–1214, Feb. 2021.
[32] W. Qin, Y. Qiu, C. Sun, and Y. Feng, "Modified SVPWM scheme for fault-tolerant control of AC-DC PWM converter," *IEEE J. Emerg. Sel. Topics Power Electron.*, vol. 9, no. 4, pp. 4715–4725, Aug. 2021.
[33] L. M. Halabi, I. M. Alsofyani, and K. B. Lee, "Multiple-fault-tolerant strategy for three-phase hybrid active neutral point clamped converters using enhanced space vector modulation technique," *IEEE Access*, vol. 8, pp. 180113–180123, 2020.
[34] H. K. Ku and J. M. Kim, "Multiple open-switch faults detection and fautls tolerant method of three-level three-phase NPC active rectifier," in *Proc. 39th Annu. Conf. IEEE Ind. Electron. Soc.*, 2013, pp. 1062–1067.
[35] J. S. Lee and K. B. Lee, "An open-switch fault detection method and tolerance controls based on SVM in a grid-connected T-type rectifier with unity power factor," *IEEE Trans. Ind. Electron.*, vol. 61, no. 12, pp. 7092–7104, Dec. 2014.
[36] K. A. Corzine and J. R. Baker, "Reduced-parts-count multilevel rectifiers," *IEEE Trans. Ind. Electron.*, vol. 49, no. 4, pp. 766–774, Aug. 2002.
[37] C. Sui, Y. He, and M. Chen, "Analysis of current distortion of three-phase voltage source rectifiers and its application in fault diagnosis," *IEEE Access*, vol. 8, pp. 4065–4075, 2020.
[38] Z. Jian-Jian, C. Yong, C. Zhang-Yong, and Z. Anjian, "Open-switch fault diagnosis method in voltage-source inverters based on phase currents," *IEEE Access*, vol. 7, pp. 63619–63625, 2019.
[39] W. Zhang, D. Xu, P. N. Enjeti, H. Li, J. T. Hawke, and H. S. Krishnamoorthy, "Survey on fault-tolerant techniques for power electronic converters," *IEEE Trans. Power Electron.*, vol. 29, no. 12, pp. 6319–6331, Dec. 2014.

Mingyun Chen was born in Zhejiang, China, in 1996. She received the B.S. degree in electrical engineering from Northeastern University, Qinhuangdao, China, in 2019. She is currently working toward the Ph.D. degree in electrical engineering in Wuhan University, Wuhan, China.

Her research interests include condition monitoring, fault diagnosis, and fault-tolerant control for power converters.

Yigang He (Member, IEEE) received the M.S. degree from Hunan University, Changsha, China, in 1992, and the Ph.D. degree from Xi'an Jiaotong University, Xi'an, China, in 1996, both in electrical engineering.

From 2006 to 2011, he worked as the Director with the Institute of Testing Technology for Circuits and Systems, Hunan University. From 2011 to 2017, he worked as the Head of the School of Electrical Engineering and Automation, Hefei University of Technology, Hefei, China. He currently works as the Vice-Head with the School of Electrical Engineering and Automation, Wuhan University, Wuhan, China. His research interests include power electronic circuit theory and its applications, testing and fault diagnosis of analog and power electronic circuits, electrical signal detection, and intelligent signal processing. He has authored/coauthored more than 300 journal and conference papers which were included more than 1000 times in Science Citation Index of American Institute for Scientific Information. He was the Vice President of China's Energy Institute of Science and Technology, the Vice President of Anhui Scientists Entrepreneurs Association, and the Director of the State Local Joint Engineering Laboratory for renewable energy grid technology.